

**Large-scale soil electrical conductivity
patterns of two electromagnetic
induction and two direct current systems**

BACHELOR-THESIS

Deadline: 01.10.2019

**Forschungszentrum Jülich, Institut für Bio- und Geowissenschaften,
Agrosphäre (IBG3)**

Name: Tobias Ganther
Student ID: 354742
Bachelor Program: Georesources Management
First Examiner: Dr. phil. nat., Professurvertreterin Gabriele Marquart
Second Examiner: Dr. Christian von Hebel
Supervisor: Dr. Christian von Hebel

Abstract

Mobile electromagnetic induction (EMI) and direct current (DC) systems can be used to measure large-scale soil apparent electrical conductivity (EC_a, [mS/m]) patterns. The EC_a is relevant for precision agriculture, for example, which is related to adapt the application rates to the specific soil parameters such as water content, texture, and salinity changes at certain locations. However, the EC_a values measured with EMI can only be considered qualitative because outer influences such as GPS, hand-held, and data cables close to the system shift the measured values, while the DC data can be considered quantitative. Multi-coil EMI systems with up to six coils are light (few kg) and can be combined to measure many depths of investigation (DOI). The DC systems with up to six DOI's are heavy (> 100 kg), which limits combination possibilities. Since EMI data can be calibrated, this thesis investigates the use of EMI and DC to obtain quantitative large-scale EC_a patterns for a 15.8 ha large test site near Einbeck (Germany). In particular, two EMI systems were combined to measure simultaneously at nine DOIs and two mobile DC systems with up to four DOIs were used. The EMI data of the nine coils were calibrated using data of few (six) vertical electrical soundings distributed over the field. The obtained quantitative large-scale EC_a values were regridded using a nearest neighbor interpolation and compared to the mobile DC data interpolated to the same grid. The calibrated EMI data provided similar large-scale EC_a patterns as well as lateral and vertical EC_a variations. The mean absolute differences between four similar DOIs of the EMI and DC systems were maximum 15 mS/m. This shows that carefully calibrated EMI data can be used to provide quantitative soil information, which can consequently be used to inform farming management systems and improve precise crop production.

Contents

1	Introduction	1
2	Geoelectrical theory	5
2.1	Electromagnetic Induction (EMI)	5
2.2	Direct current (DC)	8
3	Study site	11
4	Materials and methods	15
4.1	EMI systems	15
4.1.1	CMD-MiniExplorer	15
4.1.2	Topsoil Mapper	16
4.2	DC systems	17
4.2.1	Geophilus	17
4.2.2	VerisU3 Soil Scanner	18
4.2.3	Lippmann resistivity meter	19
4.3	Large-scale EMI and DC measurements, and soil data aquisition	20
4.4	Data processing	22
4.4.1	Calibration of EMI data	22
4.4.2	Filtering and interpolation of large-scale EMI data	23
5	Results and discussion	25
5.1	EMI calibration results	25
5.2	Large-scale soil apparent electrical conductivity (ECa) patterns	27

5.2.1	CMD-MiniExplorer	27
5.2.2	Topsoil Mapper	28
5.2.3	Geophilus	30
5.2.4	VerisU3 Soil Scanner	32
5.3	Analysis of large-scale EC _a pattern	33
5.3.1	Similarities of EMI and DC data	33
5.3.2	Statistical EC _a pattern analysis	35
6	Conclusions	39
7	Outlook	41
8	Bibliography	43
A	Additional soil information	47
A.1	Grain size analysis	47
A.2	Soil properties	48
A.3	Grain size and EC _a relation	50
B	Additional calibration data	51
B.1	VES inversion results of all locations	51
C	Large-scale EC_a measurement and processing data	55
C.1	Measurement data of the 10 m and 5 m tracks	55
C.1.1	Uncalibrated and filtered CMD-MiniExplorer data	55
C.1.2	Topsoil Mapper	59
C.1.3	Geophilus	61
C.1.4	VerisU3 Soil Scanner	63
C.2	Interpolated 10 m and 5 m track data	64
C.2.1	Calibrated CMD-MiniExplorer Data	64
C.2.2	Topsoil Mapper	67
C.2.3	Geophilus	69
C.3	Difference Plots of the interpolated track data	71

C.4 Photos of the EMI and DC systems and survey pictures	78
List of Figures	83
List of Tables	87

1 | Introduction

For agricultural purposes and especially for precision agriculture, knowledge of the subsurface structure and the soil distribution is of utmost importance to improve farming by using precise nutrient and water application rates at specific locations. Since the soil acts as water and nutrient storage, precision farming needs detailed information of the field specific soil structure in both the lateral and vertical direction. Vertically, the upper few soil meters, where most of the roots are located [Amelung et al., 2018], play a major role for precise crop production. In this shallow part of the subsurface, geophysical methods such as electromagnetic induction (EMI) and direct current (DC) can potentially help to non-invasively investigate the soil patterns at the specific locations, which can consequently improve agricultural field management.

Due to their inductive nature, the EMI method enable contactless and rapid large-scale measurements, which has been used in several areas such as agriculture and forestry [Allred and Daniels, 2008], environmental monitoring, groundwater protection, geological mapping [Klaus et al., 2007], civil engineering [Beamish, 2011], and archaeology [Saey et al., 2013]. The portable EMI systems that carry the entire unit of transmitter (Tx) and receiver (Rx) in a rigid boom provide a measure of the subsurface apparent electrical conductivity (ECa). The ECa depends on different soil properties such as the clay content, the water content, and/or the mineral content [Robinson et al., 2008; Abdu et al., 2008]. Thus, large-scale ECa patterns successfully help to upscale soil texture [Doolittle and Brevik, 2014; Saey et al., 2013] and help to interpret soil water content distributions within a catchment [Abdu et al., 2008; Robinson et al., 2008].

Commercially available and relatively light-weight (few kg) multi-coil EMI systems carry up to six Rx and use one Tx to transmit a primary magnetic field with a frequency

in the kHz-range. This field induces eddy currents in the subsurface, which in turn generate secondary magnetic fields [Keller and Frischknecht, 1966]. These are picked-up at the multiple Rx that are increasingly separated in the rigid boom to simultaneously measure over increasing depth ranges. The ratio of the secondary and primary magnetic field is related to EC_a, which is a weighted average value of the subsurface electrical conductivity distribution.

The electrical DC resistivity methods measure EC_a by introducing a direct current, i.e., a current in the Hz-range, into the subsurface using two electrodes while two potential electrodes measure voltage. This galvanic method was developed for exploration geophysics and is an established technique for subsurface characterization in many applications. For example, DC methods are successfully used to observe the subsurface structures [Romero-Ruiz et al., 2019], to monitor soil water changes [Abdu et al., 2008], to explore groundwater reservoirs [Robinson et al., 2008] and landfills [Kearey, 2002]. DC measurements are often performed using multiple electrodes along lines (up to km-long) or by using few electrodes and walking to multiple locations in a field. By increasing the electrode separations, increasing depth ranges are investigated such that the DC methods also measure EC_a values (of overlapping depth ranges). This EC_a is essentially comparable to the EC_a measured with EMI because the frequency-dependency of EC_a is negligible in the Hz to kHz range [Loewer et al., 2017]. However, EMI measurements are prone to errors because of their inductive coupling to any electrical conductor surrounding the system. For example, differences in EC_a already occur when different operator measure along the same transect [Nüscher et al., 2010]. Further, the hand-held and/or the data cables in the proximity of the system are expected to influence the measurements. Thus, EMI measurements are of a qualitative nature [Binley et al., 2015].

To obtain quantitative (large-scale) EMI data, a calibration is necessary. One option to calibrate EC_a measured with EMI uses soil cores as ground truth data. This approach was successfully used by Triantafyllis et al. [2000] and Moghadas et al. [2012]. They recorded EC_a at sampling locations and calibrated those against the theoretical EMI response calculated from the true electrical conductivity distribution measured at regular depth increments of particular soil cores. However, drilling at numerous sampling

locations may be required to cover the apparent electrical conductivity distribution of the entire field. To overcome this limitation, Lavoué et al. [2010] introduced a calibration approach using data acquired by electrical resistivity tomography (ERT) making drilling obsolete. ERT data can be used together with the specifications of the EMI system as input for an electromagnetic forward model that predicts ECa. Using linear regression between the predicted and measured ECa obtains calibration factors that can be used to turn the qualitative ECa into quantitative EMI data. This approach successfully calibrates large-scale EMI data [von Hebel et al., 2014]. Since the ECa range of the complete field is needed for successful calibration, more than one ERT transects may be set up. Sticking and connecting the numerous (~ 100) electrodes in the field is time consuming such that von Hebel et al. [2018] introduced using data of four electrodes measured at several locations such that flexible data acquisitions distributed over the field are feasible. Here, the use of that calibration approach to obtain quantitative large-scale EMI data will be explored.

For large-scale DC measurements, mobile systems mounted on trailers and dragged over the field are nowadays commercially available. These heavy systems (>100 kg) investigate up to six different depth ranges [Gebbers et al., 2009; Gebbers and Lück, 2015]. The provided large-scale ECa patterns can be used for agricultural purposes, for example, such that the data quality of ECa measured with EMI and DC has been studied [Lueck and Ruehlmann, 2012]. The normalized ECa patterns of the mobile EMI and DC mapping systems were consistent. Nonetheless, large differences were present in the absolute values of the different systems. This can be potentially closed by calibrating the EMI data [von Hebel et al., 2018].

Since the DC information can be considered quantitative, the current thesis investigates the large-scale ECa patterns obtained with two mobile DC measurement systems and compares these data with the ECa distributions measured with two EMI systems. The EMI and DC measurements were performed at a 15.8 ha large test site near Einbeck (Germany). In particular, the ECa values measured with the inductively working CMD-MiniExplorer (GF-Instruments, Czech Republic) and those of the 'Topsoil Mapper' (Geoprospectors, Austria) are compared to the DC data of the 'Geophilus'

(Geophilus GmbH, Germany) and the VerisU3 (Veris Technologies, USA) systems. In addition, independent vertical electrical soundings (VES) using four electrodes were performed at twelve locations in the field, where also soil samples were taken. Using these data, the thesis hypothesizes that the large-scale ECa patterns of calibrated EMI data are similar to those of the DC systems with the benefit that the EMI systems deliver more information than the DC system.

In the next (2nd) chapter, the theoretical background of EMI and CD measurements are explained. The third chapter describes the soil characteristics of the study site. In the fourth chapter, the materials and methods will be illustrated, and the fifth chapter shows and discusses the results. In particular, the calibration of the EMI data is outlined, and the large-scale ECa patterns of the different systems are visually and statistically analyzed. The sixth chapter, finally draws the conclusions and ends with an outlook for future work.

2 | Geoelectrical theory

2.1 Electromagnetic Induction (EMI)

Electromagnetic induction (EMI) systems use a transmitter coil and one or more receiver coils to provide a measure of the electromagnetic field coupling in the shallow subsurface [CEN, 2011]. They typically operate at small coil separations and at low frequency in the kHz range. The combined separation-frequency EMI attribute is designed to provide a measure of the subsurface apparent electrical conductivity across a depth range that is governed by the coil separation and the coil orientations [Beamish, 2011].

A transmitter coil, continuously energized with a sinusoidal audiofrequency current, forms a magnetic dipole. Its primary magnetic field induces eddy currents in the conductive ground, which is illustrated in Fig. 2.1. These eddy currents generate a secondary magnetic field that is of the same frequency but with a different phase and of lower amplitude than the primary field. The primary and secondary magnetic fields are superimposed on each other and the resultant field is detected by the receiving coil [Klaus et al., 2007].

The secondary magnetic field strength depends on the ground electrical conductivity. Although these relationships are expressed by a complicated function, a linear equation can be used to estimate the relationship between the electrical conductivity and the secondary magnetic field when the coil spacing and frequency are small enough. Operation using small coil spacing, and frequency is called operation at “low induction number (LIN)”. The induction number N_b characterizes the depth of current flow inside a conductor:

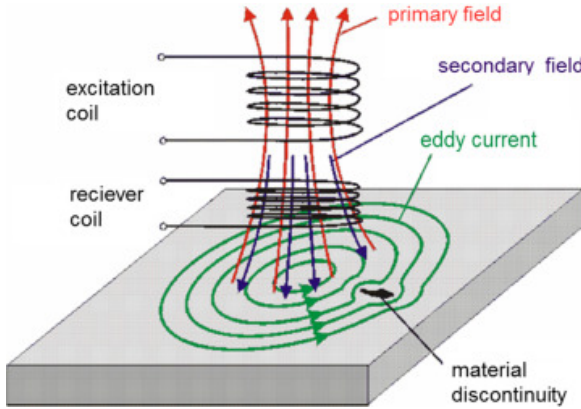


Figure 2.1: Principle of electromagnetic induction methods [Breidenstein, 2017]

$$N_b = \frac{s}{\delta} \quad \text{where} \quad \delta = \sqrt{\frac{2}{\mu_0 \omega \sigma}} \quad (2.1)$$

N_b = induction number [-]

μ_0 = permeability of free space [$\frac{N}{A^2}$]

s = coil spacing [m]

ω = angular frequency [$\frac{rad}{s}$]

δ = skin depth [m]

σ = ground electrical conductivity [$\frac{S}{m}$]

The skin depth δ is the depth where the primary magnetic field has been attenuated to $\frac{1}{e}$ (ca. 37 %) of its original strength. EMI instruments typically have several operational modes or coil configurations (see Fig. 2.2). Often coplanar coils in which both transmitter and receiver coils are either oriented horizontally (HCP) or vertically (VCP) with respect to the ground surface are used. As a rule of thumb, VCP loops sense the ground up to a depth ranges of approximately 0 to 0.75 times the coil separation while HCP loops sense depth ranges of approximately 0 to 1.5 times the coil offset [McNeill, 1980]. VCP is more sensitive to the subsurface interface. The HCP coils show a maximum sensitivity at $\sim 0.4s$ tending to zero at the interface and larger depths. The configurations complement each other regarding their sensitivity distribution as well as their depth range of investigation (DOI). Under natural conditions it can be assumed that soil can be described as a horizontally layered medium with layers of different elec-

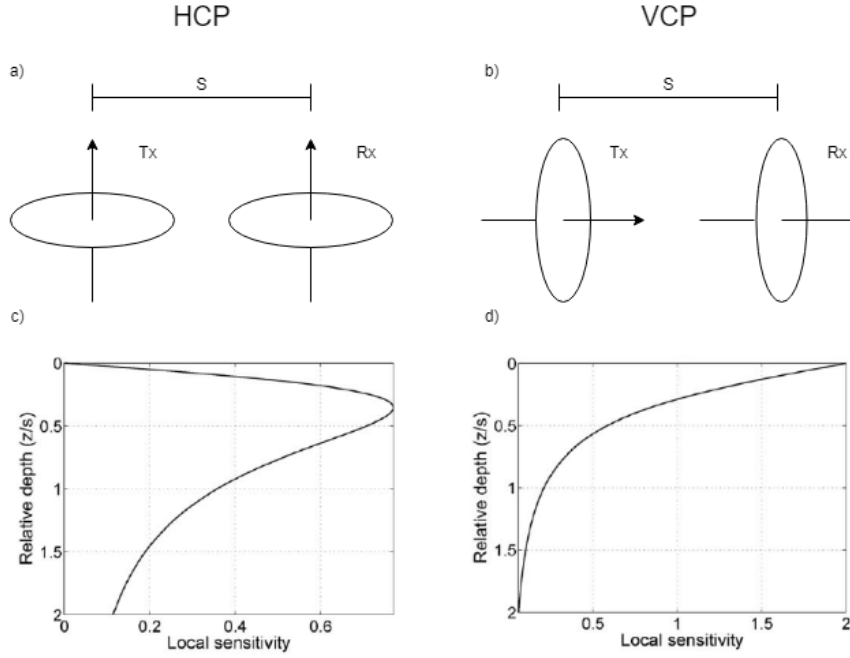


Figure 2.2: Graphic description of the a) HCP and b) VCP configurations. (S = coil spacing, Tx = transmitter coil, Rx = receiver coil) and local sensitivity functions for depth normalized to coil separation for c) HCP and d) VCP. (after McNeill [1980])

trical conductivities. Measurements over stratified soils provide a non-linear average value of the vertical electrical conductivity distribution within the DOI, the so called apparent electrical conductivity (ECa). The signal can also include layers beyond the DOI, since the DOI has been defined where the sensitivity accumulates to 70% [McNeill, 1980]. Thus, the remaining 30% can substantially contribute the ECa [von Hebel et al., 2018]. To fully describe the EM response, the Maxwell-based full solution EMI model as described in the following is used. The strength of the induced secondary magnetic field increases with increasing electrical conductivity [Keller and Frischknecht, 1966]. The secondary magnetic field, measured on a horizontally layered subsurface with an EMI system in VCP and HCP mode, can be explicitly described according to [Wait, 1982]:

$$H^{HCP} = 1 - s^2 \int_0^\infty R_0 J_1(s\lambda) \lambda d\lambda \quad (2.2)$$

$$H^{VCP} = 1 - s^3 \int_0^\infty R_0 J_0(s\lambda) \lambda^2 d\lambda \quad (2.3)$$

J_n = Bessel Function of n^{th} order R_0 = reflection coefficient

The reflection coefficient R_0 between the different layers and their pertaining layer thickness can be obtained recursively beginning with $R_{n+1} = 0$, since it is considered that no fields are generated below the lowest half space [Ward et al., 1988].

$$R_n = \frac{\frac{\Gamma_n - \Gamma_{n+1}}{\Gamma_n + \Gamma_{n+1}} R_{n+1} \exp(-2\Gamma_{n+1} h_{n+1})}{1 + \frac{\Gamma_n - \Gamma_{n+1}}{\Gamma_n + \Gamma_{n+1}} R_{n+1} \exp(-2\Gamma_{n+1} h_{n+1})} \quad (2.4)$$

$$\Gamma_n = \sqrt{\lambda_n^2 \gamma_n^2} ; \quad \gamma_n^2 = \sqrt{j\omega \mu_0 \sigma_n} \quad (2.5)$$

λ^2 = radial wavenumber [-] ω = angular frequency [$\frac{rad}{s}$]

γ_n^2 = propagation constant [-] μ_0 = magnetic susceptibility of free space [$\frac{N}{A^2}$]

$j^2 = -1$ = imaginary unit [-] σ_n = electrical conductivity of the n^{th} layer [$\frac{S}{m}$]

This quasi-static forward model is exact for the low frequencies where EMI systems operate. At these f (\sim kHz), a diffusive regime is present and the field only propagates due to conduction currents [Keller and Frischknecht, 1966].

2.2 Direct current (DC)

Direct current (DC) resistivity methods use sources of current to produce an electrical potential field in the ground. A current is introduced through two electrodes and the potential field is measured using two other electrodes. Since the potential, the current introduced through the electrodes, and the electrode configuration are known, the apparent resistivity of the ground can be determined [Klaus et al., 2007]. In the remainder of this thesis, the DC methods are expressed in terms of ECa (as used for EMI), since the electrical conductivity is the reciprocal of the electrical resistivity.

To investigate the subsurface, different electrode configurations can be used. In general, by changing the distance between source electrodes (A and B) and measurement

electrodes (M and N) different depth ranges of are measured that can be estimated by AB/2 [Nostrand and Cook, 1966].

The sensitivity distribution for a horizontally layered subsurface of several electrode configurations is shown in Figure 2.3. The DC methods show a peak sensitivity at certain depths and no sensitivity at zero and larger depths [Roy and Apparao, 1971]. Note that this curve behaves similar as the sensitivity distribution of HCP coils of an EMI system. This allow expecting that multiple DC measurements using shorter and larger electrode spacings deliver similar subsurface information as the EMI method.

Beside the other possible electrode configurations as shown in Figure 2.3, the DC systems used in this work use the Schlumberger configurations for the VES and VerisU3 measurements as well as the equatorial Dipole-Dipole configuration for the Geophilus system.

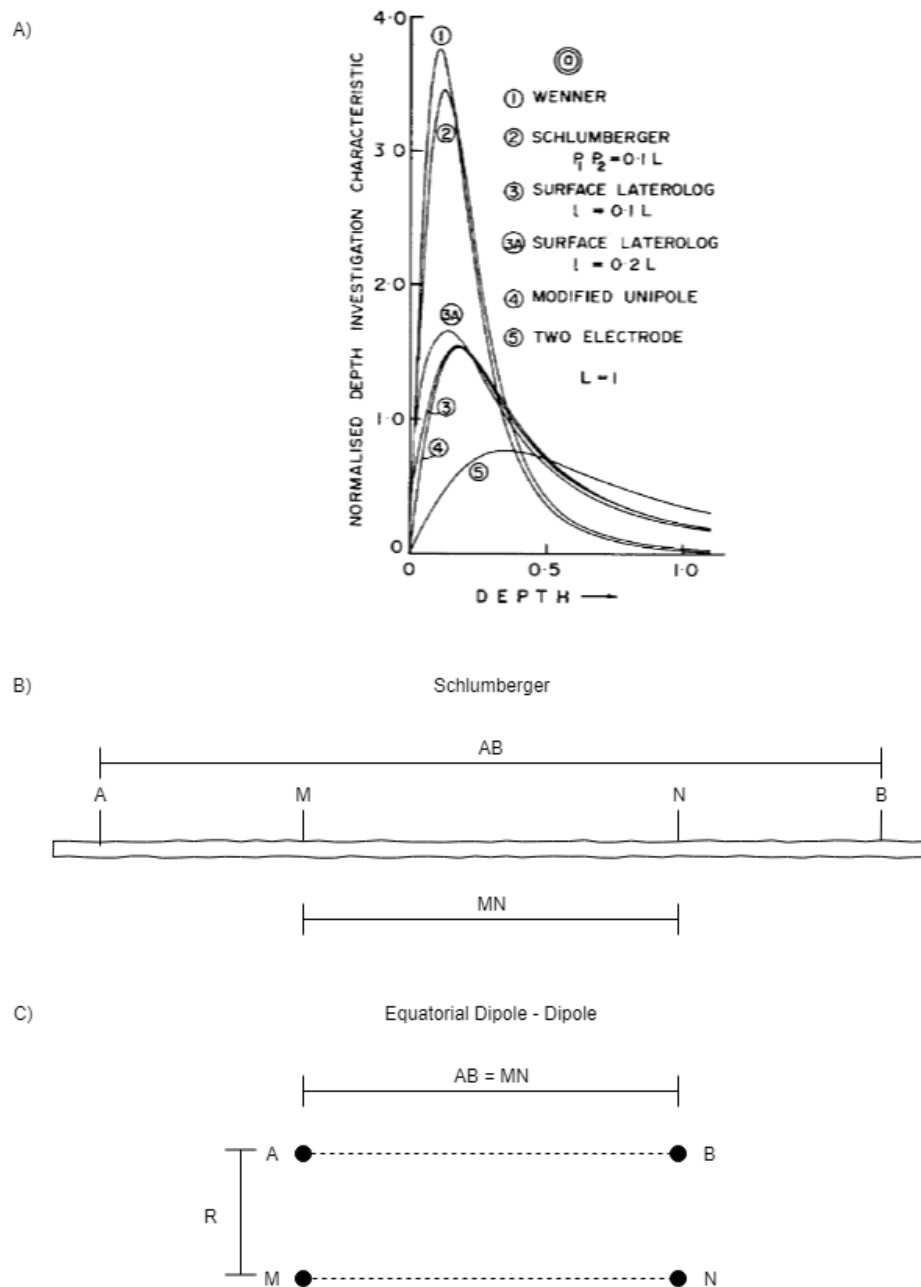


Figure 2.3: a) Depth investigation characteristics of various array configurations [Roy and Apparao, 1971], b) electrode configuration for a Schlumberger and c) an equatorial Dipole-Dipole array)

3 | Study site

The study site is located near the village of Dörrigsen, a southern part of the city of Einbeck in the southern region of Lower Saxony (Germany) and is used for agriculture. Satellite images of the test site are shown in Figures 3.1 a) and b). Comparing the image of 2018 in Fig. 3.1 a) with the image of 2000 in Fig 3.1 b), tracks in N-S as well as W-E direction are visible which, were caused by the agricultural machines. The newer tracks seem to be the tracks in W-E direction because only this direction can be seen in the recent satellite images on Google Earth.

The test site has a size of 15.8 ha and is part of the Einbeck-Markoldendorfer basin. The top sediments consist of quaternary sediments, which are mostly glacial loess deposits from the Pleistocene [Brunotte, 1978]. The underlying rocks are triassic Buntsandstein sandstones with a distinct red color. The spatial soil type distributions presented in Figure 3.2 a) show that Luvisols (Parabraunerde) dominate the test site. In the north west of the test site Cambisols (Braunerden) and partly Chernozems are present, while in the northern part of the test site Anthrosols (Kolluvisol) are present. The Cambisols in the middle of the field are shallower than the surrounding soils. According to the GK25 map shown in Figure 3.2 b) the northwestern part of the test site contains a higher clay content than the rest of the field.

To improve the soil description at the test site, soil samples were extracted up to 90 cm depth at 12 locations using a Pürkhauer soil sampling system. These were analyzed in 30 cm depth increments as outlined in the Appendix A and the grain size distribution is summarized in two tables which can also be found in the appendix. Overall, the soil type of the test site is classified as silt loam according to the USDA textural classification (Figure 3.3).



Figure 3.1: Satellite images of the test site taken on a) the 10th of June 2018 and b) the 31th of December 2000 (Google Earth)

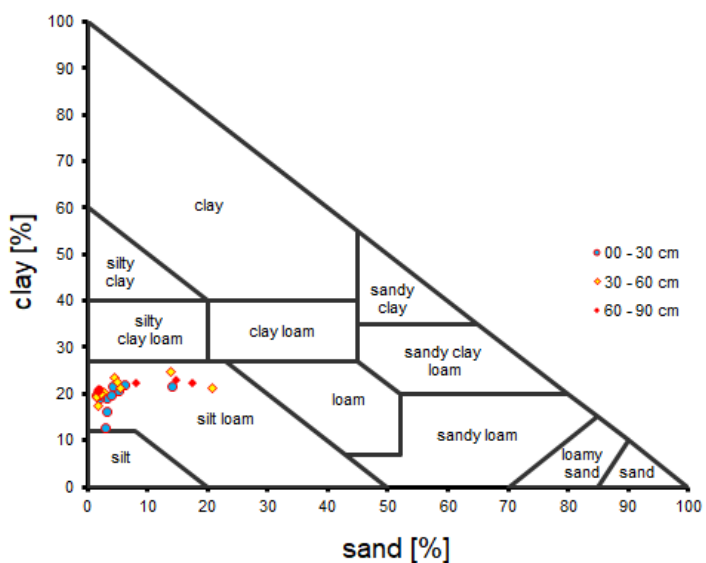


Figure 3.3: Grain size distributions of the soil samples sorted by depth

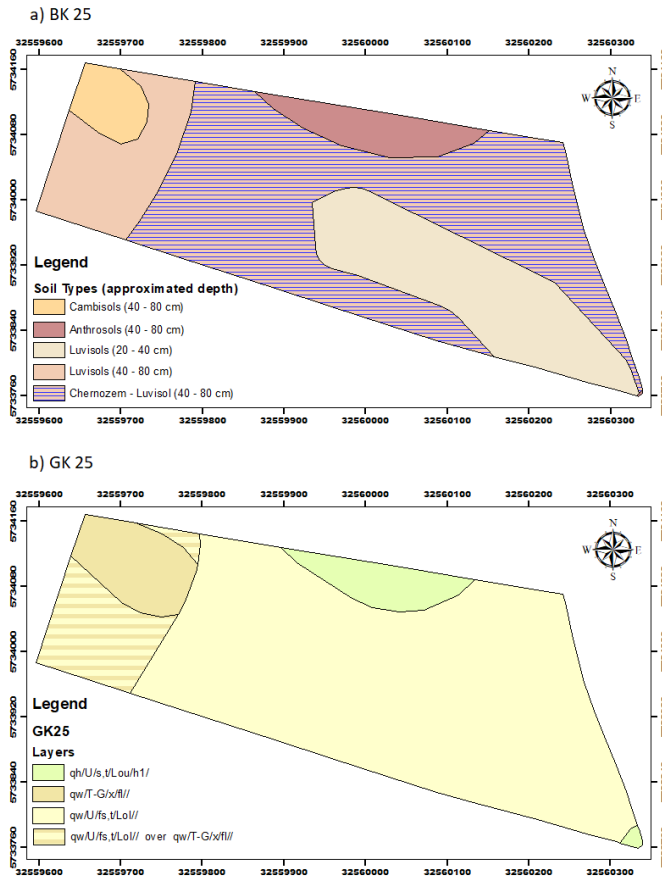


Figure 3.2: a) soil type map based on the national BK25 map and b) grain distribution map based on the national GK25 map, scale 1:25000

The grain size distribution of the soil samples is homogeneous with low horizontal variations. The sand content is slightly increased by the locations 1 and 6. On these locations it was not possible to take samples from depths below 60 cm. The grain distributions of these locations show that the deeper the samples the higher the sand content. Apparently, the sand descends from the bedrock, which is red Buntsandstein. During the grain size analysis, the distinct red color of the Buntsandstein was observed in the sand sieves confirming this assumption. Globally however, the entire test site is loess dominated.

In the field, a vertical change of the consistency of the soil could be observed. The upper areas of the soil were predominantly brown and not very plastic, while in the lower areas the soil was greyish and also more plastic indicating a higher clay content. However, a significantly higher clay content was not measured in the grain size analysis.

4 | Materials and methods

4.1 EMI systems

In this work, EMI systems of two manufactures were used for the large-scale measurements. The 'Institute of Bio- and Geosciences Agrosphere (IBG-3)' of the Forschungszentrum Jülich, provided two CMD-MiniExplorer systems of GF-Instruments (Brno, Czech Republic), which are detailed next. Then, the Top Soil Mapper (Geoprospectors, Austria) that has been ordered by KWS SAAT SE & Co. KGaA to investigate the behavior of the different systems will be described.

4.1.1 CMD-MiniExplorer

The EMI were performed using a regular CMD-MiniExplorer (ME) and a custom-built CMD-SpecialEdition (SE). Both EMI systems are mounted on a custom-made plastic sled to provide a close and constant distance to the soil. The hand-held to control the EMI system is attached to a vertically aligned plastic stick for each sled. Also a differential Global Positioning System (GPS) produced by Trimble (Sunnyvale, USA) is attached to track the data points that were continuously recorded using a 5 Hz sampling rate. The setup of sleds is shown in Figure 4.1. The ME-system uses three receiving coils with an offset of 0.32 m, 0.71 m and 1.18 m to the transmitter, while the SE-system has six receiving coils with offsets of 0.35 m, 0.50 m, 0.71 m, 0.97 m, 1.35 m and 1.80 m. The ME operates at 30 kHz and was used in HCP mode, while the SE works at 25.17 kHz and was used in VCP mode. Due to the different frequencies, both systems can be used simultaneously such that EC_a values of nine coil configurations as shown in Table 4.1 where measured in one go.

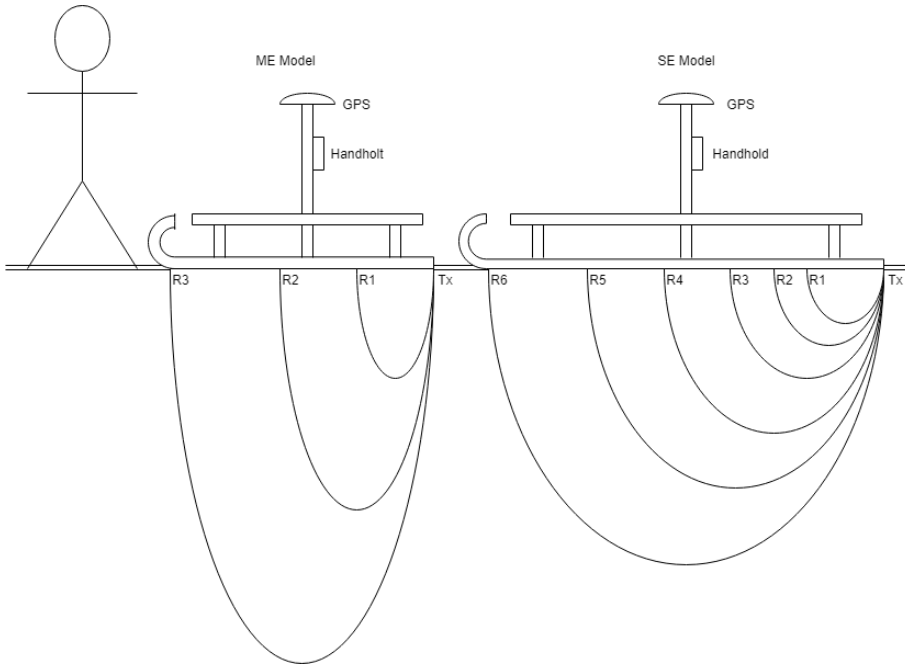


Figure 4.1: Sketch of the construction of both sledges and their DOIs

Table 4.1: Coil characteristics of the sleds

System	Orientation	Separation [m]	DOI [m]
ME	HCP	0.32	0 - 0.48
ME	HCP	0.71	0 - 1.10
ME	HCP	1.18	0 - 1.77
SE	VCP	0.35	0 - 0.26
SE	VCP	0.49	0 - 0.38
SE	VCP	0.71	0 - 0.53
SE	VCP	0.97	0 - 0.73
SE	VCP	1.35	0 - 1.01
SE	VCP	1.80	0 - 1.35

4.1.2 Topsoil Mapper

The Topsoil Mapper is a commercial EMI system for agricultural purposes. The system consists of four receiver coils with 0.5 m, 0.7 m, 0.9 m, and 1.1 m distance to the transmitter coil. The maximal investigation depth range is 1.10 m with the coils positioned

30 cm above the ground. Due to sparse information provided by the company, here it is concluded that all coils were orientated in HCP during the survey. Furthermore, a GPS system provides the spatial positions of the acquired data. The Topsoil Mapper gets fixed on agricultural machines in order to measure the apparent electrical conductivity [Geoprospectors, 2019].

Table 4.2: Coil characteristics of the Topsoil Mapper

Coil separation [m]	Orientation	DOI [m]	DOI - offset [m]
0.5	HCP	0 - 0.75	0 - 0.45
0.7	HCP	0 - 1.05	0 - 0.75
0.9	HCP	0 - 1.35	0 - 1.05
1.1	HCP	0 - 1.65	0 - 1.35

4.2 DC systems

Besides the EMI systems, two DC systems of two manufacturers were used for the large-scale measurements. In the following sections, the Geophilus Electricus (Geophilus GmbH, Germany) and the VerisU3 (Veris Technologies, USA) will be described. These systems have been ordered by the KWS company. In addition, the IBG-3 of the Forschungszentrum Jülich provided a Lippmann earth resistivity meter 'Model 10W - 4 Point Light' (Schaufing, Germany). The Lippmann system was used to perform the VES measurements, which were used for the calibration of the CMD-MiniExplorers data.

4.2.1 Geophilus

Geophilus Electricus (termed here Geophilus) is a DC system for mapping the ECa of soils using rolling electrodes instead of static ones like in VES or ERT measurements. The system consists of an equatorial dipole-dipole array (six pairs of galvanic coupling electrodes). The rolling electrodes simultaneously measure amplitude and phase data at four frequencies ranging from 1 mHz to 1 kHz. This thesis uses the provided ECa value for each of the six equatorial dipole-dipole configurations. The system's design

and technical specifications allow for measuring these parameters at five depths of up to ca. 1.5 m. A GPS provided spatial information up to a precision of 10 cm. The following Figure 4.2 shows a sketch of the fundamental setup of the Geophilus system. Table 4.3 contains the most important technical information of the system [Lueck and Ruehlmann, 2012].

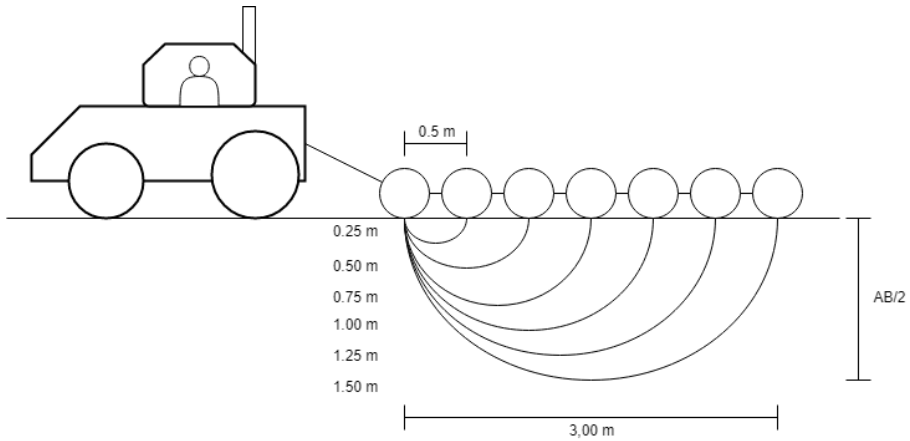


Figure 4.2: Sketch of the Geophilus construction and its DOIs

Table 4.3: Electrode spacings AB and its respective DOIs

AB [m]	0.5	1.00	1.50	2.00	2.50	3.00
DOI [m]	0 - 0.25	0 - 0.50	0 - 0.75	0 - 1.00	0 - 1.25	0 - 1.50

4.2.2 VerisU3 Soil Scanner

The VerisU3 Soil Scanner is a multipurpose system capable of measuring electrical conductivity variation, organic matter variation and acidity, which requires further processing and auxiliary information. In this thesis, the EC_a values of the one Schlumberger electrode configuration are used. The Veris uses four metal wheels function as mobile electrodes. The discs are positioned in an array. The inner two discs are used for the direct current emission into the ground while the outer two discs measure the voltage (see Figure 4.3). The investigation depth of the Veris U3 goes from 0 to 60 cm. A GPS is also used to position the measured data [Vantage-Agrometius, 2019].

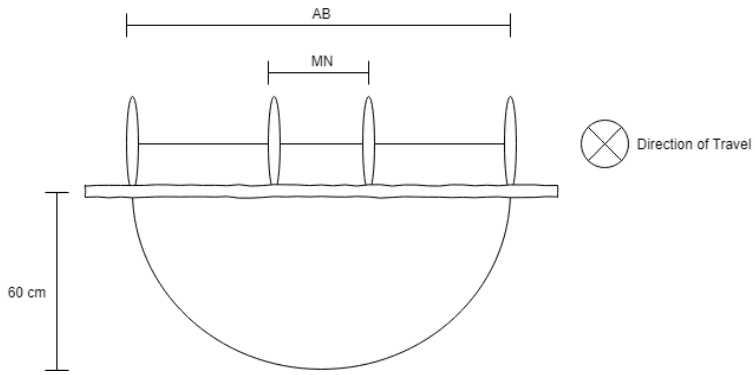


Figure 4.3: Sketch of the disc positions of the VerisU3

Table 4.4: The VerisU3 electrode spacing AB and its respective DOI

AB [m]	1.20
DOI [m]	0 - 0.60

4.2.3 Lippmann resistivity meter

For the VES measurements, the earth resistivity meter '4point light 10W' from the German company Lippmann was used. It measures the phase shift between the current injected into the ground and the voltage seen at the potential electrodes. It has adequate power to drive vertical electrical sounding up to $AB/2 = 1000$ m. There are 16 frequencies from 0.2 to 30 Hz available. The output current varies between 1 mA – 100 mA in 8 steps. An output voltage up to 380 V can be used. The maximal output power is 10W in AC. A resolution up to 50nV / 0.1 mrad can be obtained [Lippmann, 2015]. VES is used for detecting vertical variations of electrical conductivity in the subsurface beneath the electrode's location. The principle of VES is based on the fact that the wider the current electrode separation the deeper the current penetration. During the measurement of an array, the electrode spacings are constantly being increased in order to measure in different depths of investigation (see Figure 4.4). VES provides the subsurface ECa at one specific location that can be used for horizontally layered inverse-modeling at that location. The following Table 4.5 shows the electrode spacings used for the VES measurements.

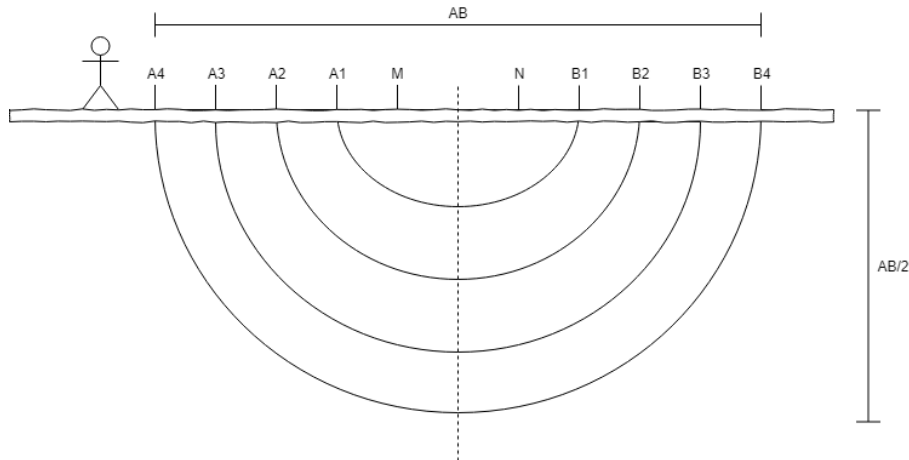


Figure 4.4: Sketch of the principle of VES measurements. Every step the electrode spacing increases increasing the DOI

Table 4.5: Electrode spacings used for the VES measurements

AB/2 [m]	5.00	4.50	4.00	3.50	3.00	2.75
MN/2 [m]	1.00					
AB/2 [m]	2.50	2.25	2.00	1.75	1.50	
MN/2 [m]	0.50					
AB/2 [m]	1.25	1.00	0.75	0.5		
MN/2 [m]	0.25					

4.3 Large-scale EMI and DC measurements, and soil data aquisition

The large-scale EMI and DC measurements were performed on the 26.03.2019. The measurements were performed in two track distances which are illustrated in Figure 4.5. In the east-west direction, the tracks were 10 m apart. In the north-south direction, the distance was 5 m. The temperature during the measurements was relatively constant between 8 and 12°C. The weather conditions during the measurement remained unchanged. The measurements with the CMD-MiniExplorer, the Vertical Electrical Sounding measurements and the grain size analysis were performed by the Forschungszentrum and the acquired data further processed.

Before performing the main measurement with the CMP-MiniExplorer the systems were warmed up for 30 minutes in order to acclimate to the surrounding temperature. While measuring along the transect, the sleds were pulled by a tractor with a rope and a distance of at least 7 m to the operator to minimize the influence of the tractors metal on the measurements. The distance between sleds was 4.4 m for the same reasons. The sampling interval was set to 0.2 s, which records one ECa data point approximately every 20 cm. On 12 locations, VES measurements were performed, where the arrays headed in east-west direction. Furthermore, soil samples were taken on all 12 locations every 30 cm until the final depth of 90 cm.

The the measurements of the Topsoil Mapper, Geophilus and VerisU3 as well as the soil sampling were not performed by the Forschungszentrum. The data of these systems were provided by external sources.

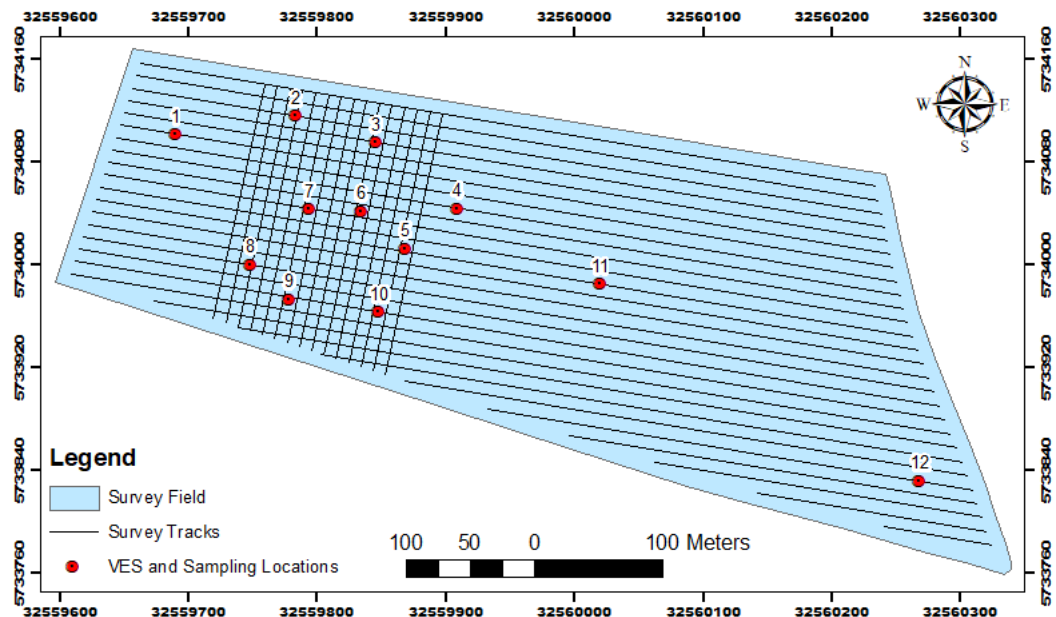


Figure 4.5: Map of the Einbeck test site showing the tracks of the EMI and DC measurements and the VES locations

4.4 Data processing

The measured EMI data of the CMD-MiniExplorer as well as the measured VES data and the information acquired from the soil samples were processed here, since the data of the Topsoil mapper, the Geophilus, and the Veris systems were provided as end-product by the respective company.

4.4.1 Calibration of EMI data

To calibrate the large-scale EC_a patterns and obtain quantitative EMI data, collocated EMI and VES measurements were performed at the calibration locations CL1 to CL12 shown in Figure 4.5 which ideally cover the observed EC_a ranges of the entire test site [von Hebel et al., 2018]. At each CL, the EMI instruments recorded EC_a values for around 60 s and their mean was used for calibration against predicted EC_a values. To predict EC_a values, the VES data of each CL were inverted using the code of von Hebel et al. [2018] to obtain the respective vertical electrical conductivity distribution. These were inserted into the Maxwell-based full solution EMI forward model [Keller and Frischknecht, 1966; Wait, 1951] along with the EMI instrument specifications to predict the EC_a values for the specific calibration location. A linear regression of measured and predicted EC_a values results in coil configuration-specific calibration factors that turn the qualitative EC_a maps into quantitative data.

First the inversions were performed for models using 2 to 5 layers, which were checked against auxiliary data such as the ground truth soil sampling to determine the most plausible amount of layers.

After these preprocessing steps, the inversion was performed with the chosen amount of layers and the chosen VES locations. As a result, the predicted values were plotted against the measured EC_a to perform the linear regression and obtain the calibration factors.

4.4.2 Filtering and interpolation of large-scale EMI data

The measured CMD-MiniExplorer data were processed based on the filters as described next. After a first view on the raw data, boundaries of maximum and minimum EC_a values were defined in order to remove extremely high and low outlier values. For the test site investigated here, the boundaries of -5 and 60 mS/m were selected. After that the so called 'histogram filter' was applied. The histogram filter bins the EMI data into 15 equally spaced containers and computes the percentage of the data within each container. Containers which contain less than 0.5% were removed assuming that these values do not match into the remaining majority of assumingly correct field data. In addition, strongly laterally varying EC_a values, where the deviation exceeds 1.5 mS/m between the actual measurement and adjacent recordings were removed. Finally, the filtered data were smoothed. Due to the applied filters, the EMI data sets did not have the same length anymore [von Hebel et al., 2014]. Therefore, the data were regridded using nearest neighbor interpolation with a grid size of 1.0 m in both spatial directions. This grid was used to interpolate the data of the TopSoil Mapper, of Geophilus, and of Versis provided the commercial companies. In that way, all EMI and DC data can be compared at the same locations as performed in the next chapter.

5 | Results and discussion

5.1 EMI calibration results

For the calibration of the large-scale ECa values measured with the combined ME and SE systems, few collocated EMI and vertical electrical sounding data were recorded at twelve calibration locations distributed over the ca. 700 m by 200 m (15.8 ha) large Einbeck test site. To reconstruct the subsurface layering from the VES data, these were inverted for two, three, four- and five layer models at each calibration location. The visual inspection showed that the four and five layers were too complex having multiple insertions of adjacent high and low electrically conductive layers. Many of these layers were very thin (~ 10 cm) and seemed implausible such that it was concluded that the four and five layer inversion results were not appropriate to explain the subsurface at the Einbeck test site.

A comparison between the two- and three layer inversions showed that the two layer models were not able to reproduce the measured VES data as shown in Figure B.3. As a result of this, the three layer inversion results were selected, since these reproduced the measured VES data and were in most agreement with the geological observations. However, similarly to the four- and five layer inversions, the three layer inversion also reconstructed very thin layers at six locations such that six locations were selected for the final calibration plots. In order to improve the calibration here and in future work, geological knowledge should be incorporated in the code developments. Summing up, six VES data points for a three layered medium remained for the EMI data calibration (CL1, CL4, CL7, CL9, CL10 and CL11). The calibration of six out of the nine configurations showed high correlation with coefficients of determination (R^2) around 0.9, except for the VCP71 ($R^2 = 0.76$).

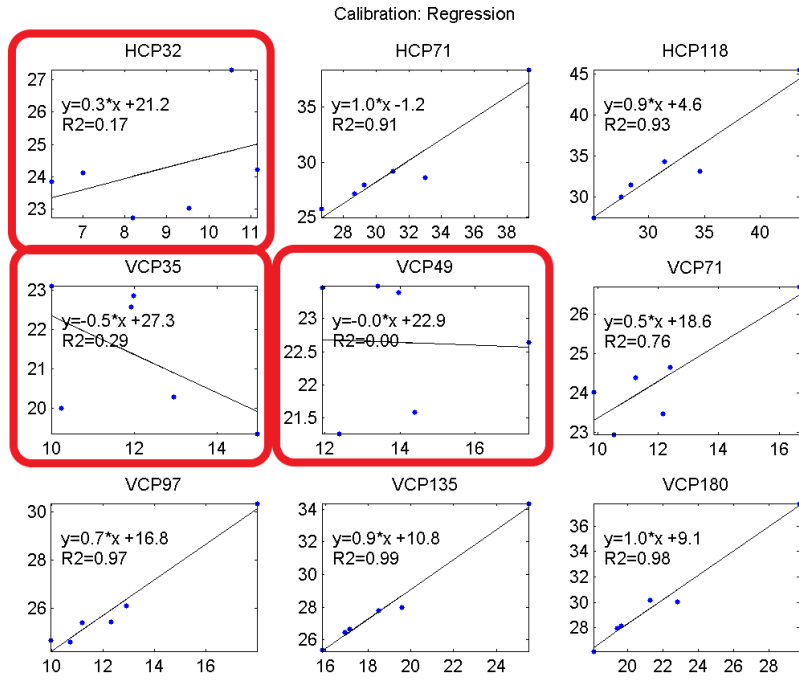


Figure 5.1: Linear regression of VES ECa predicted (x-axis) and EMI ECa measured values (y-axis) in [mS/m] for all coil configurations

The three configurations with the lowest DOI (framed in red) showed R^2 lower than 0.3 indicating that linear regression could not be performed to calibrate these data. Instead, a simple shift correction was applied using the mean differences between the predicted and measured ECa values. The shift correction values are listed in the following Table:

Table 5.1: Applied parameters for the shift correction

Configuration	mean EMI [mS/m]	mean VES [mS/m]	VES-EMI [mS/m]
HCP 32	8.8	24.2	15.4
VCP 35	12.0	21.4	9.4
VCP 49	13.9	22.6	8.7

The differences were larger for the HCP than for the VCP coil configurations, which indicates that the field setup has a larger influence on the HCP than on the VCP coils. These respectively produce a vertical and a horizontal magnetic dipole that are stronger and lesser influenced by the GPS and the hand-held that are at a height of 1 m and 0.6 m above the EMI system, respectively. Nonetheless, the influence is substantial such that calibration using linear regression or a simple shift as introduced here is needed.

5.2 Large-scale soil apparent electrical conductivity (ECa) patterns

5.2.1 CMD-MiniExplorer

After the calibration and the filtering, the data were interpolated and plotted. The resulting maps showing the final calibrated ECa maps are discussed as follow. The maps of the measured ECa tracks are shown in the appendix C.

Globally the electrical conductivity of the soil is relatively homogeneous. The absolute range of the ECa is relatively small especially if the size of the test site also gets taken into account. Especially the VCP35 of 0-0.3 m as shown in Figure 5.2(a) show only minor variations with higher ECa values at small areas in the northwest and south.

On shallow configurations, linear and periodic structures in north-south as well as east-west direction are clearly visible, which can be seen in Figure 5.2(b) for the deeper HCP118 configuration. This coil has a lower sensitivity near the surface, which indicates that the structures mainly descend from processes near the surface. These linear structures probably descend from agricultural processes, mostly consolidation due to agricultural machines. The structures redraw the farmers driving tracks which can be verified on satellite images (see Figure 3.1). Furthermore, the north-south structures are not as strongly visible as the east west direction. Satellite images taken over a decade ago show treatment in this direction while the newer images only show treatment in east-west direction. As a result, the older structures are not as strongly visible as the newer ones. Nonetheless after all the years these structures are still visible.

On the northwestern part as well as on the southern part of the test site, ECa was measured. These structures become stronger with increasing DOI indicating that these structures are located in deeper depths not descending from agricultural processes. Globally, the electrical conductivities on the test site increase with increasing DOI as can be seen in the Figures C.10 to C.12 in the appendix. A clear statement about the heritage of the structures cannot be made. Soil samples were taken until a depth of 0.90 m, but the main part of the structure seems to be located below this depth. Thus, the samples taken in the field can only give limited information about the vertical variation.

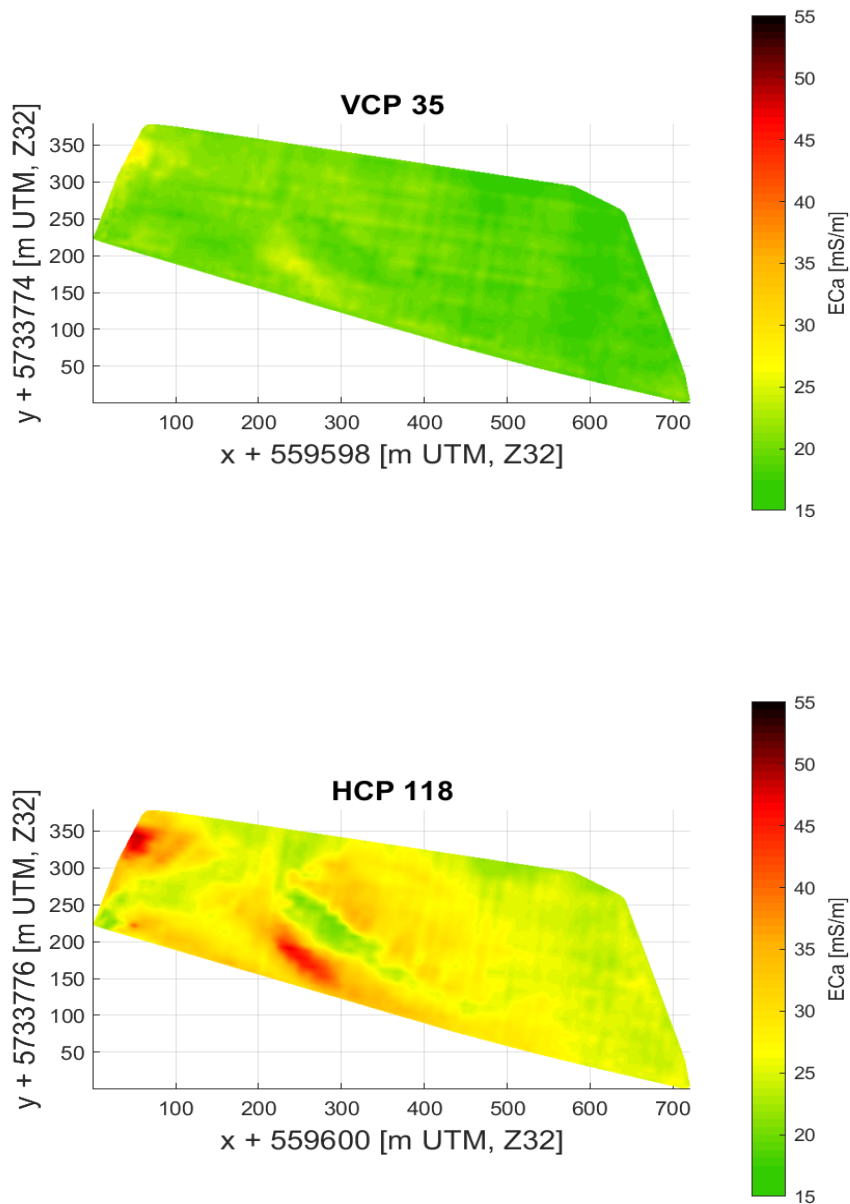


Figure 5.2: ECa distribution of the 10 m tracks of VCP35, DOI 0 - 0.26 m (above) and HCP118, DOI 0 - 1.77 m (below)

5.2.2 Topsoil Mapper

Qualitatively, the main patterns which were already identified on the CMD data were also visible on the Topsoil Mapper. However, the resolution of these maps is lower.

The location of the deeper structures match to the CMD patterns as well as the linear shallow structures. Furthermore, there is a significant difference between the EC_a of different measurement times. The EC_a which were measured later show a higher electrical conductivity compared to EC_a which were measured earlier on the same position. The reason behind this observation is a temperature shift which was caused by a higher air temperature of 10°C during the day heating up the systems thus increasing the measured electrical conductivities.

The absolute electrical conductivities are more than 10 times higher than the measured EC_a of the CMD instruments (see Figure 5.3). The reason is the position where the Topsoil Mapper is attached on the tractor. The distance between the main body of the tractor and the topsoil mapper is approximately 0.5 m (see Figure C.26). As a result, the measured EC_a values are highly increased and do not represent the real EC_a of the subsurface. Nonetheless, the range of the EC_a values does not exceed 45 mS/m. This range of EC_a is very well in accord to the EC_a range of the CMD-MiniExplorer.

The company provides a program to process the data, which has not been available for this thesis. A quantitative comparison between the Topsoil Mapper and the remaining systems is therefore not possible.

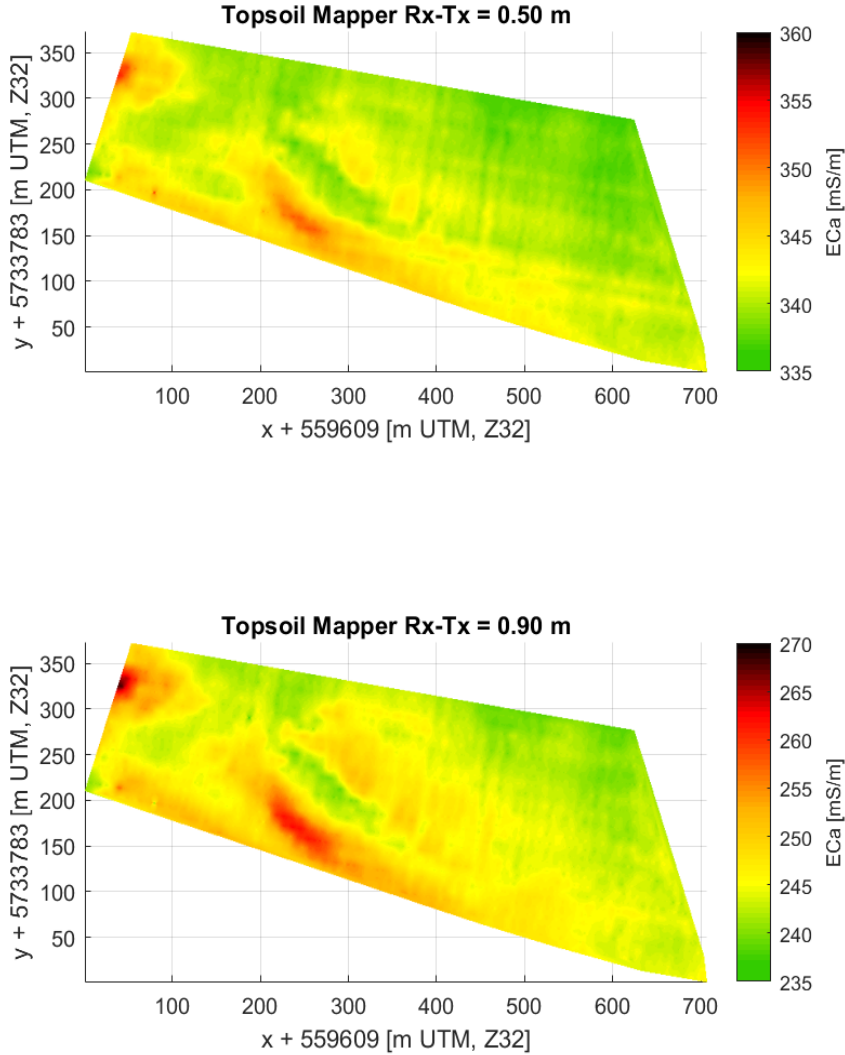


Figure 5.3: ECa distribution of the Topsoil Mappers 10 m tracks, above: Rx-Tx 0.5 m, DOI 0 - 0.45 m, below Rx-Tx 0.9 m, DOI 0 - 1.05 m

5.2.3 Geophilus

In the interpolated large-scale ECa maps of the Geophilus, the same observations of structures like for the previous systems can be made. Vertical ECa variations are also similar as well as the areal distribution of the structures. The structure of the patterns however was less smooth compared to the other EMI and DC systems. The borders of certain electrical conductivity areas are relatively edgy. Some of the electrical conductiv-

ity patterns even build small 'islands' with relatively crisp shifts of electrical conductivity. In Figure 5.4 this observation can be very well seen. The traces of the tracks also show higher contrasts to the unconsolidated areas. This observation might be caused by the galvanic coupling, where the electric current prefers to flow along the unconsolidated areas while due to its inductive nature EMI simply penetrates the consolidated 'isolator' including this area more into the ECa measurement.

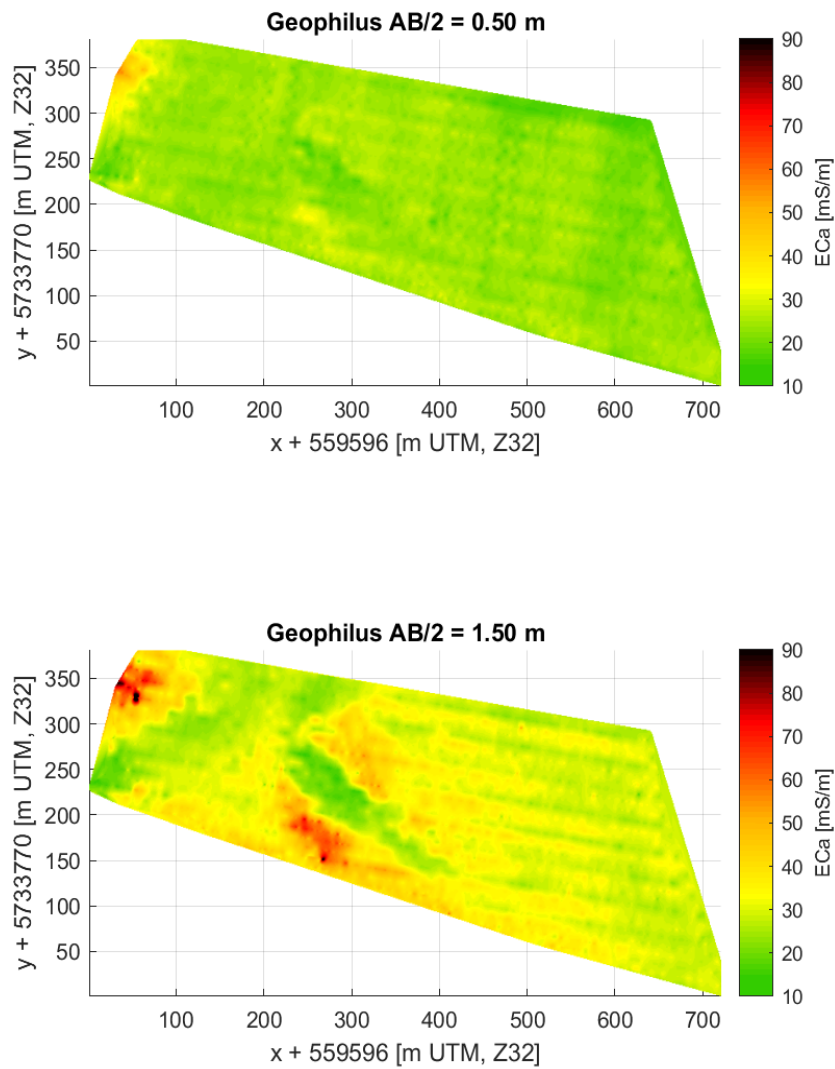


Figure 5.4: ECa distribution of the Geophilus 10 m tracks, above DOI = 0 - 0.5 m, below DOI = 0 - 1.5 m

Quantitatively there are also deciding differences. The more conductive structures show larger ECa than de CMD plots. The extreme ECa values exceed 100 mS/m which is in no geologically reasonable context. Apparently the Geophilus tends to measure way higher ECa values on highly conductive structures while on the other hand the lower conductive areas show values matching the values of the VerisU3 while the values of the CMD are slightly lower globally.

5.2.4 VerisU3 Soil Scanner

For the VerisU3 only the 5 m tracks of the field were measured. The results are similar to the results of the calibrated CMD and the Geophilus data. In Figure 5.5 linear structures in north-south direction are clearly visible, structures in west-east direction on the other hand are only lightly visible. There are only data for a DOI of 0.60 m. Thus it is not possible to make statements about vertical ECa variations.

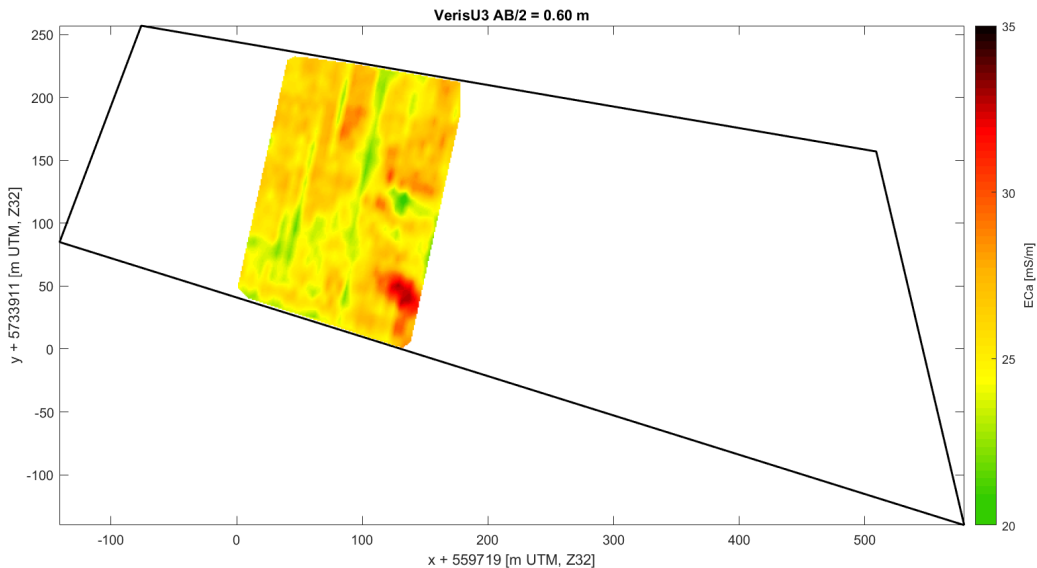


Figure 5.5: ECa distribution of the VerisU3 5 m tracks, DOI = 0 - 0.6 m

Furthermore, the VerisU3 shows unlike the Geophilus no dotty patterns or 'islands' of higher electrical conductivity but a smoother ECa distribution, while the global distribution of the ECa as well as the structures in north-south direction are very much similar. The electrical conductivities on the highly conductive structure in the south however are not as high as in the Geophilus patterns.

In comparison to the patterns of the VCP71 (similar DOI) coil of the calibrated CMD data, the horizontal and vertical structures are not as fine on the VerisU3 patterns as they are on the VCP71 pattern. Moreover, the highly conductive structure shows higher variation than the rest of the measured test site but not as extreme as in the Geophilus patterns.

5.3 Analysis of large-scale ECa pattern

For further investigation difference plots between the CMD and both DC systems were made in order to compare the calculated plots in regard of spatial, relative and absolute differences. In addition, the horizontal mean standard deviation of all DOIs were acquired for a detailed statistical analysis. Furthermore, vertical standard deviation plots were made in order to distinguish vertically heterogeneous areas.

5.3.1 Similarities of EMI and DC data

As Figure 5.6 exemplarily shows, globally the differences between the Geophilus and the CMD data are below 5 mS/m except for the electrically highly conductive areas. Similar results were obtained for the comparison with the VerisU3 also shown in Figure 5.6. The differences between the CMD data and the ECa of the DC systems increase with increasing DOI because of the large increase of the ECa values of the Geophilus. In larger DOIs the differences in the highly conductive structures were more severe whereas the less conductive areas showed similar ECa values. Thus, the highest differences were caused by the data quality of the Geophilus data and not calibration errors. Globally however both DC systems measured slightly larger ECa than observed for the CMD data. In addition, the unsmooth character of the Geophilus patterns were practically redrawn by the difference plots. The unsmooth island like ECa distribution does not represent any geological reasonable formation. The smooth ECa patterns of the CMD-MiniExplorer on the other hand do represent a way more authentic picture of the underground with the more continuous and uncrisp changes of electrical conductivity.

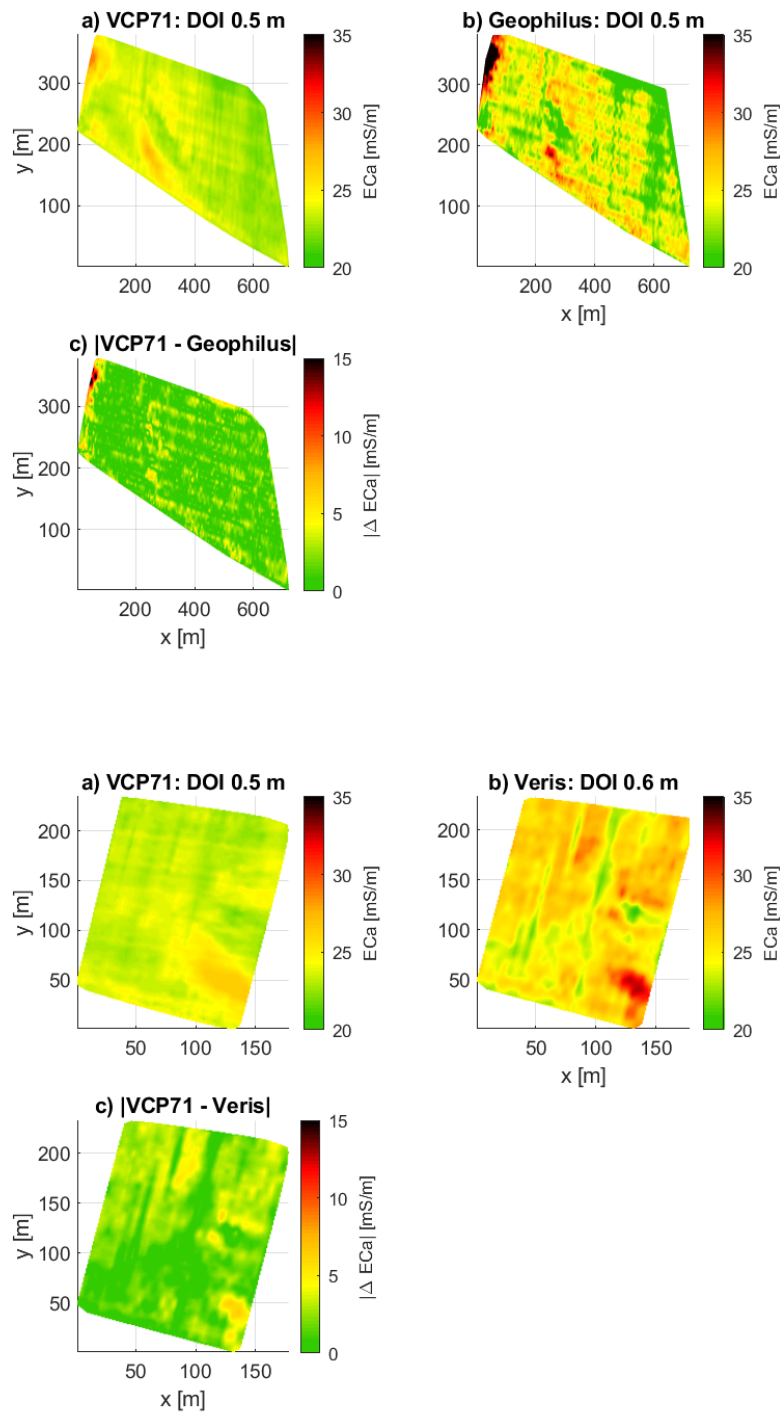


Figure 5.6: Above: difference plot between CMD and Geophilus, DOI 0 - 0.5 m, Below: Difference plot between CMD and VerisU3, DOI 0 - 0.6 m

5.3.2 Statistical ECa pattern analysis

The mean ECa of every DOI were acquired and the mean values of the different systems compared to each other. A comparison of the standard deviations between the CMD and the Geophilus shows visually similar results. First, the areal mean standard deviation increases with further DOI (see Table 5.2). Secondly, the vertical standard deviations of both systems increase in areas with higher ECa values as Figure 5.7 shows. This observation is in accord to the previously observed vertical ECa changes because a higher changes in ECa values are caused by heterogeneities which results in higher standard deviations. Quantitatively however, the absolute ECa differences between the CMD and the Geophilus patterns also result in different standard deviations. Because of the bigger ECa varieties of the Geophilus, the resulting standard deviations are much higher, especially the vertical ones as the comparison between Figure 5.7 clearly shows.

Table 5.2: Vertical changes of mean ECa and standard deviations [mS/m]

Configuration	DOI	mean	stdev	AB/2	mean	stdev
HCP 32	0.48	21.3672	2.367	0.25	18.6918	2.5787
HCP 71	1.10	25.3938	2.9034	0.50	23.9509	2.9540
HCP 118	1.77	27.5519	3.8696	0.75	27.4840	3.8728
VCP 35	0.26	19.6447	1.5908	1.00	29.6772	5.1081
VCP 49	0.38	20.3912	1.6916	1.25	30.8340	6.0119
VCP 71	0.53	23.4319	0.931	1.50	32.4117	7.1963
VCP 97	0.73	23.575	1.4509			
VCP 135	1.01	24.6507	2.0896			
VCP 180	1.35	26.6773	2.7484			

The following Tables 5.3 and 5.4 show the mean ECa values of similar DOIs. Essentially, the observations are similar to the difference plots. The higher the DOI, the higher is the mean difference between the Geophilus and the CMD data. In almost every DOI which was compared against each other, the DC systems show higher mean ECa values.

Table 5.3: Mean CMD and Geophilus ECa and standard deviations [mS/m] of similar DOIs [m]

AB/2	mean	stdev	DOI	mean	stdev	stdev (EMI - DC)
0.25	18.6918	2.5787	0.26	19.6447	1.5908	0.9529
0.50	23.9509	2.9540	0.48	21.3672	2.367	-2.5837
0.50	23.9509	2.9540	0.53	23.4319	0.931	-0.519
0.75	27.484	3.8728	0.73	23.575	1.4509	-3.909
1.00	29.6772	5.1081	1.10	25.3938	2.9034	-4.2834
1.00	29.6772	5.1081	1.01	24.6507	2.0896	-5.0265
1.25	30.834	6.0119	1.35	26.6773	2.7484	-4.1567

Table 5.4: Mean CMD and VerisU3 ECa and standard deviations [mS/m] of similar DOIs [m]

AB/2	mean	stdev	DOI	mean	stdev	stdev (EMI - DC)
0.60	25.7306	1.6216	0.53	23.689	0.7674	-2.0417

Between both DC systems, the trend of lateral and vertical changes fit perfectly. As Table 5.5 shows, the areal mean ECa of the VerisU3 ($AB/2 = 0.6$ m) is located between the respected values of the Geophilus in regard of adjacent DOI. This result shows that both systems that work with similar technology also provide similar results. Nonetheless, the standard deviation of the VerisU3 is smaller than the standard deviations of the Geophilus DOIs next to the VerisU3.

Table 5.5: Vertical changes of mean ECa and standard deviations [mS/m] of both DC systems

AB/2	mean	stdev
0.25	20.2506	1.6264
0.50	24.8158	2.6275
0.60	25.7306	1.6216
0.75	27.1875	4.1253
1.00	29.4413	5.2484
1.25	30.1998	7.9561
1.50	31.1745	9.5622

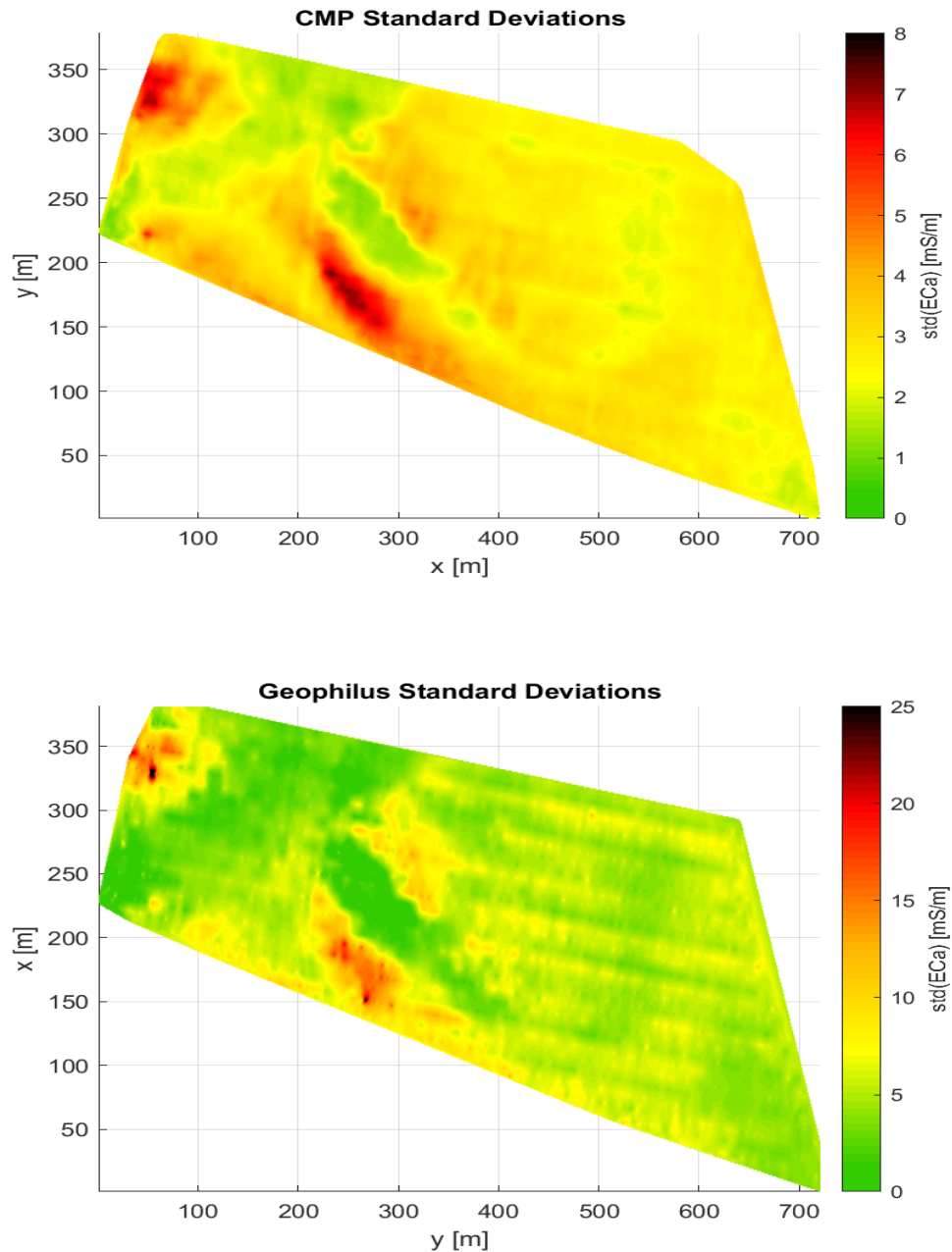


Figure 5.7: Vertical standard deviations of the CMD-MiniExplorer (above) and the Geophilus (below)

6 | Conclusions

This thesis compared and analyzed, large-scale ECa patterns of EMI and DC systems. Visually, the lateral patterns of all EMI and DC systems were similar. The linear periodic structures of the agricultural machines as well as the highly electrically conductive structures were visible on all ECa maps of every system. However, there are major differences in respect of the smoothness between the EMI and the DC systems. The EMI systems show higher smoothness than the DC systems, especially compared to the Geophilus. The results of the EMI systems seem more reasonable than the DC results when considering the geological knowledge that let expect smooth soil changes.

Furthermore, the ECa values of the DC systems, especially of the Geophilus are highly increased on highly conductive areas while the CMD data showed lower ECa values. The dimension of the Geophilus values highly exceeds geological reasonable values while the differences between the CMD and VerisU3 values are still in an acceptable range. It was not possible to identify the reason behind the high ECa values of the Geophilus. In comparison with the soil textures, it seems that range the CMD data showed most expectable results. Taking the homogeneous traits of the soil samples into account, this allows concluding that extreme ECa values cannot be measured at the Einbeck test site. For the calibration, the combination of both the linear regression as well as the shift correction seem to successfully calibrate the nine EMI coils, since the quantitative ECa values were similar as those obtained with the DC systems. Higher differences can only be observed for the area of the highly conductive underground structures by using the Geophilus. These differences are likely due the Geophilus and not the applied calibration, since the Versis performed similar as the calibrated CMD at these areas.

The success to generate quantitative ECa values over entire areas using VES data at few locations, EMI becomes an efficient tool for big scale measuring of quantitative electrical

conductivity. This can further gain information of subsurface properties such as soil moisture or clay content. A huge advantage of the EMI systems is the high flexibility. EMI systems are light (few kg) and are thus easy to combine, to transport and to build up in the field. Mobile DC systems on the other hand are way heavier making it more difficult perform combined measurements of different systems, to transport and to build them up in the field.

7 | Outlook

Based on the results of this work, further actions can be performed in order to gain more information about the Einbeck test site. The acquired EMI data can now be used to perform a quantitative inversion in order to build a model of the soil structure and layering. Following this information, the agricultural land use can be adapted to increase its efficiency. A more specified land use can increase harvests while decreasing the use of resources such as water, fertilizers or pesticides. Parameters influencing the use of such resources are grain size and soil moisture. Thus, it is beneficial to gain spatial as well as vertical information about these properties. A higher clay content often correlates with soil moisture and can have a storage function for nutrients. Because clay contents correlate with higher EC_a values, the EMI data can also be used to gain such information about these essential soil properties.

Based on the results obtained so far, the test site will be further investigated. It is planned to perform additional ground penetrating radar (GPR) measurements, to improve depth-to-bedrock estimation. Beside these measurements, invasive drillings such as geological core soundings might be useful to obtain further information of the deeper structures. Non-invasive ERT measurements along the structures might also provide complementary information to validate the EC_a range of the calibrated EMI data obtained with the approach performed in this thesis.

8 | Bibliography

(2011): Cen Workshop Agreement, Best Practice Approach For Electromagnetic Induction (emi) Measurements Of The Near Surface, EUROPEAN COMMITTEE FOR STANDARDIZATION. [5](#)

Abdu, H., Robinson, D. A., Seyfried, M., Jones, S. B. (2008): Geophysical imaging of watershed subsurface patterns and prediction of soil texture and water holding capacity, Water Resources Research, doi:<https://doi.org/10.1029/2008WR007043>. [1](#), [2](#)

Allred, B., Daniels, J. J. E. M. (2008): Handbook of agricultural geophysics, CRC Press. [1](#)

Amelung, W., Blume, H.-P., Fleige, H., Horn, R., Kandeler, E. (2018): Scheffer/Schachtschabel Lehrbuch der Bodenkunde, Springer-Verlag GmbH, https://www.ebook.de/de/product/31053619/wulf_amelung_hans_peter_blume_heiner_fleige_rainer_horn_ellen_kandeler_scheffer_schachtschabel_lehrbuch_der_bodenkunde.html. [1](#)

Beamish, D. (2011): Low induction number, ground conductivity meters: a correction procedure, Journal of Applied Geophysics, 75. [1](#), [5](#)

Binley, A., Hubbard, S. S., Huisman, J. A., Revil, A., Robinson, D. A., Singha, K., Slater, L. D. (2015): The emergence of hydrogeophysics for improved understanding of subsurface processes over multiple scales., Water Resources Research, 51, 3837–3866, doi:[10.1002/2015WR017016](https://doi.org/10.1002/2015WR017016). [2](#)

Breidenstein, O. (2017): 2 - Sensors, data storage and communication technolo-

- gies, in: Cyber-Physical and Gentelligent Systems in Manufacturing and Life Cycle, edited by Denkena, B., Mörke, T., pp. 7 – 278, Academic Press, doi: <https://doi.org/10.1016/B978-0-12-811939-6.00002-9>, <http://www.sciencedirect.com/science/article/pii/B9780128119396000029>. 6, 83
- Brunotte, E. (1978): Zur quartären Formung von Schichtkämmen und Fußflächen im Bereich des Markoldendorfer Beckens und seiner Umrahmung (Leine-Weser-Bergland), Göttinger Geographische Abhandlungen, 72. 11
- Doolittle, J. H., Brevik, E. C. (2014): The use of electromagnetic induction techniques in soils studies, Geoderma, 223-225, 22–45, doi:10.1016/j.geoderma.2014.01.027. 1
- Gebbers, R., Lück, E. (2015): Comparison of geoelectrical methods for soil mapping, doi:10.13140/RG.2.1.3435.9201. 3
- Gebbers, R., Lück, E., Dabas, M., Domsch, H. (2009): Comparison of instruments for geoelectrical soil mapping at the field scale, Near Surface Geophysics. 3
- Geoprospectors (2019): official website, internet page, <https://www.topsoil-mapper.com>. 17
- Kearey, P. (2002): An Introduction To Geophysical Exploration, Wiley-Blackwell, https://www.ebook.de/de/product/3831005/philip_kearey_an_introduction_to_geophysical_exploration.html. 2
- Keller, G. V., Frischknecht, F. C. (1966): Electrical Methods in Geophysical Prospecting, Pergamon Press. 2, 7, 8, 22
- Klaus, V., Gerhard, K., Hans-Jürgen, L. (2007): Environmental Geology Handbook of Field Methods and Case Studies, Springer Verlag. 1, 5, 8
- Lavoué, F., Jan van der Kruk, J. R., F. André D., M. J., A. Huisman, S. L., L. Weiermüller, J. V. H. V. (2010): Electromagnetic induction calibration using apparent electrical conductivity modelling based on electrical resistivity tomography, Near Surface Geophysics, Vol 8, 553 – 561. 3
- Lippmann, G. M. (2015): 4-point light 10W, Earth Resistivity Meter, Kornacker 4 D-

94571 Schaufling. [19](#)

Loewer, M., Günther, T., Igel, J., Kruschwitz, S., Martin, T., Wagner, N. (2017): Ultra-broad-band electrical spectroscopy of soils and sediments—a combined permittivity and conductivity model, *Geophysical Journal International*, 2010, 1360–1373,, doi: doi:10.1093/gji/ggx242. [2](#)

Lueck, E., Ruehlmann, J. (2012): Resistivity Mapping With Geophilus Electricus — Information About Lateral And Vertical Soil Heterogeneity, Elsevier. [3](#), [18](#)

McNeill, J. D. (1980): Electromagnetic Terrain Conductivity Measurement At Low Induction Numbers, Geonics Limited. [6](#), [7](#), [83](#)

Moghadas, D., F. Andre, J. H. B. J. v. d. K., H. Vereecken, S. L. (2012): Electromagnetic induction antenna modelling using a linear system of complex antenna transfer functions, *Near Surf. Geophys.*, 10, 237 – 247. [2](#)

Nostrand, R. V., Cook, K. L. (1966): Interpretation of resistivity data, Washington, U.S. Govt. Print. Off. [9](#)

Nüsch, A.-K., Dietrich, P., Werban, U., Behrens, T. (2010): Acquisition and reliability of geophysical data in soil science, 19th World Congress of Soil Science, Soil Solutions for A Changing World. [2](#)

Robinson, D. A., A. Binley, N. C., F. D. Day-Lewis, T. P. A. F., V. J. S. Grauch, R. K., M. Knoll, V. L., R. Miller J., N. L., Pellerin K., S. L. S. (2008): Advancing process-based watershed hydrological research using near-surface geophysics: a vision for, and review of, electrical and magnetic geophysical methods, *Hydrological Processes*, 22, doi:10.1002/hyp.6963. [1](#), [2](#)

Romero-Ruiz, A., Linde, N., Keller, T., & Or, D. (2019): A Review Ofgeophysical Methods For Soilstructure Characterization, *Reviewsof Geophysics*, 56, 672–697. [2](#)

Roy, A., Apparo, A. (1971): Depth Of Investigation In Direct Current Methods, *Geophysics*, 36. [9](#), [10](#), [83](#)

Saey, T., Stichelbaut, B., Bourgeois, J., Van Eetvelde, V., VanMeirvenne, M. (2013):

An interdisciplinary non-invasive approach to landscape archaeology of the Great War, Archaeological Prospection, 20. [1](#)

Triantafyllis, J., Laslett, M., McBratney, A. B. (2000): an electromagnetic induction instrument to measure salinity in soil under irrigated cotton, Soil Sci. Soc. Am. J., 64, 1009 – 1017. [2](#)

Vantage-Agrometius (2019): Veris U3 Bodenscanner, official internet page, <https://www.vantage-agrometius.nl/de/produkt/veris-u3-bodemscanner/>. [18](#)

von Hebel, C., Sebastian, R., Achim, M., Huisman Johan, A., Pramod, K., Harry, V., van der Kruk Jan (2014): Three-dimensional imaging of subsurface structural patterns using quantitative large-scale multiconfiguration electromagnetic induction data, Water Resources Research, 50. [3](#), [23](#)

von Hebel, C., Matveeva, M., Verweij, E., Rademske, P., Kaufmann, M. S., Brogi, C. (2018): Understanding Soil and Plant Interaction by Combining Ground-Based Quantitative Electromagnetic Induction and Airborne Hyperspectral Data, Geophysical Research Letters, 45. [3](#), [7](#), [22](#)

Wait, J. R. (1951): Transient Electromagnetic Propagation In A Conducting Medium, Geophysics, 16, 231. [22](#)

Wait, J. R. (1982): Geo-electromagnetism, publisher unknown, 37. [7](#)

Ward, S. H., Hohmann, G. W., Nabighian, M. N. (1988): Electromagnetic theory for geophysical applications, vol. 1, Electromagnetic methods in applied geophysics. [8](#)

A | Additional soil information

A.1 Grain size analysis

For the 12 Locations, where the VES measurements were performed, soil samples in three different depth ranges were taken. With these samples, grain size analysis after DIN ISO 11277 were performed.

First the samples dried in an oven at 105°C. The samples were dry sieved in order to remove grains over the size of 2 mm. After that the samples were grinded and further prepared for the sedimentation analysis. The sand fraction was removed using a 0,063 mm sieve. The silt and clay contents were measured in the following step using the Sedimat 4-12 via density measurements.

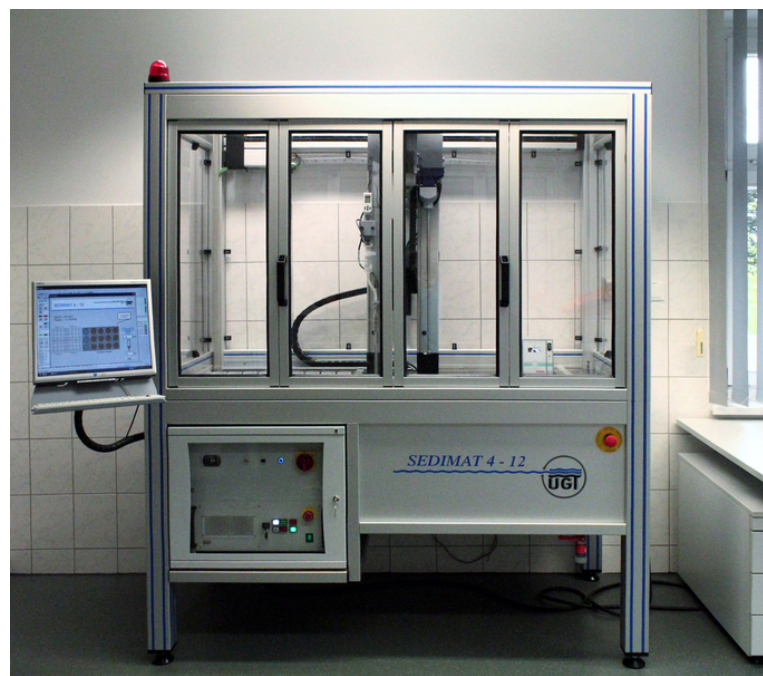


Figure A.1: Picture of the Sedimat 4-12 (UGT 2019)

A.2 Soil properties

Table A.1: Grain size distributions of calibration locations 1 - 6

location	clay [%]	f. silt [%]	m. silt [%]	c. silt [%]	sand [%]	sum [%]
CL1 0 - 30cm	21.59	6.26	13.11	44.84	14.20	100
CL1 30 - 60cm	21.11	7.20	13.81	37.19	20.69	100
CL1 60 - 90cm	-	-	-	-	-	-
CL2 0 - 30cm	20.58	5.54	19.58	48.94	5.37	100
CL2 30 - 60cm	21.17	4.34	20.82	48.11	5.56	100
CL2 60 - 90cm	22.35	6.40	17.48	36.32	17.44	100
CL3 0 - 30cm	21.56	5.91	19.30	49.02	4.21	100
CL3 30 - 60cm	23.57	5.25	19.72	47.03	4.43	100
CL3 60 - 90cm	22.38	5.73	18.78	44.99	8.12	100
CL4 0 - 30cm	19.21	5.63	19.45	53.72	2.00	100
CL4 30 - 60cm	19.92	5.51	20.53	52.20	1.84	100
CL4 60 - 90cm5	21.80	5.97	21.14	49.74	2.07	100
CL5 0 - 30cm	19.10	6.68	20.30	50.54	3.39	100
CL5 30 - 60cm	22.34	5.45	18.93	48.23	5.05	100
CL5 60 - 90cm	23.07	5.27	17.27	39.59	14.79	100
CL6 0 - 30cm	21.83	6.69	19.30	45.92	6.26	100
CL6 30 - 60cm	24.83	6.77	15.39	39.13	13.88	100
CL6 60 - 90cm	-	-	-	-	-	-

Table A.2: Grain size distributions of calibration locations 7 - 12

location	clay [%]	f. silt [%]	m. silt [%]	c. silt [%]	sand [%]	sum [%]
CL7 0 - 30cm	19.66	4.46	20.68	51.05	4.14	100
CL7 30 - 60cm	20.65	6.52	19.77	50.64	2.42	100
CL7 60 - 90cm	20.83	6.64	21.23	49.67	1.63	100
CL8 0 - 30cm	15.96	7.22	20.63	52.98	3.21	100
CL8 30 - 60cm	20.52	4.35	19.67	53.21	2.24	100
CL8 60 - 90cm	20.38	4.95	19.74	52.88	2.05	100
CL9 0 - 30cm	19.05	5.71	21.37	51.81	2.06	100
CL9 30 - 60cm	19.40	5.20	21.34	52.58	1.48	100
CL9 60 - 90cm	19.27	5.11	19.35	52.22	4.05	100
CL10 0 - 30cm	19.52	5.61	19.57	53.16	2.15	100
CL10 30 - 60cm	20.30	5.32	19.95	51.61	2.83	100
CL10 60 - 90cm	22.97	5.81	20.14	48.93	2.15	100
CL11 0 - 30cm	19.72	5.52	19.41	53.69	1.66	100
CL11 30 - 60cm	19.84	5.50	19.68	52.76	2.22	100
CL11 60 - 90cm	21.19	5.76	20.32	51.03	1.69	100
CL12 0 - 30cm	12.69	6.92	22.70	54.63	3.05	100
CL12 30 - 60cm	17.28	4.94	20.63	55.35	1.81	100
CL12 60 - 90cm	23.52	4.90	20.20	50.85	0.53	100

A.3 Grain size and EC_a relation

Here, the acquired EMI and DC data of the 12 locations (where the soil samples were taken) were plotted against the grain size distributions. Ideally there is some linear relationship between the grain size distributions and the electrical conductivity. The grain sizes were divided into clay, silt and sand. Such plots were built for every EMI and DC instrument.

However, the soil samples taken from the test site only show smallest variations in their grain size distributions. This is why the resulting plots do not show any significant linear correlation between the grain size distributions and the measured EC_a values. As a result, further investigations in this area are obsolete. As an example of the common relation between grain size distributions and the EC_a values Figure A.2 is shown as a global representation.

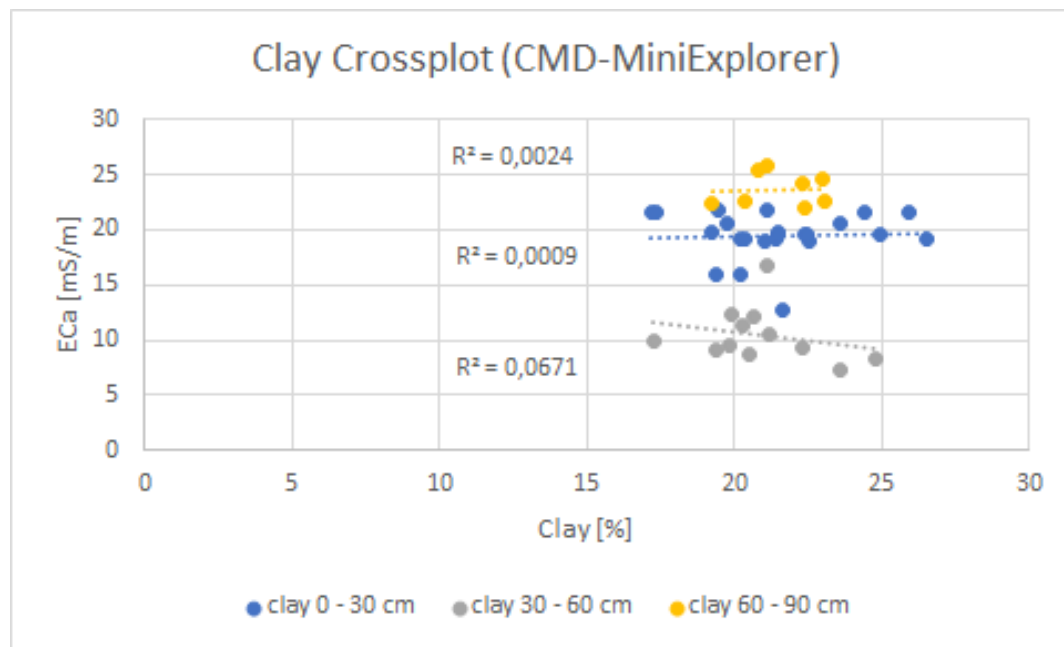


Figure A.2: Cross plot between the clay contents and the EC_a of the sleds

B | Additional calibration data

B.1 VES inversion results of all locations

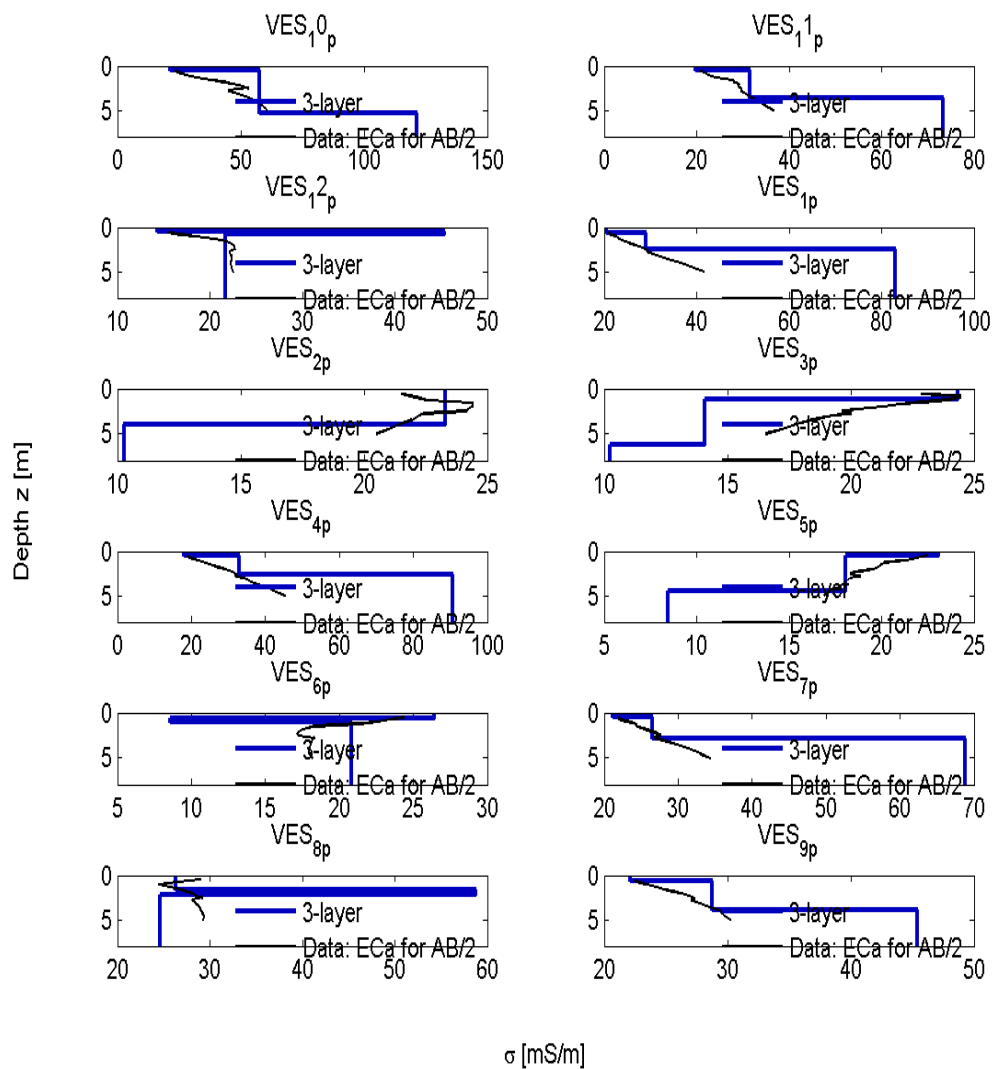


Figure B.1: Underground three layer ECa model inversion of all 12 locations

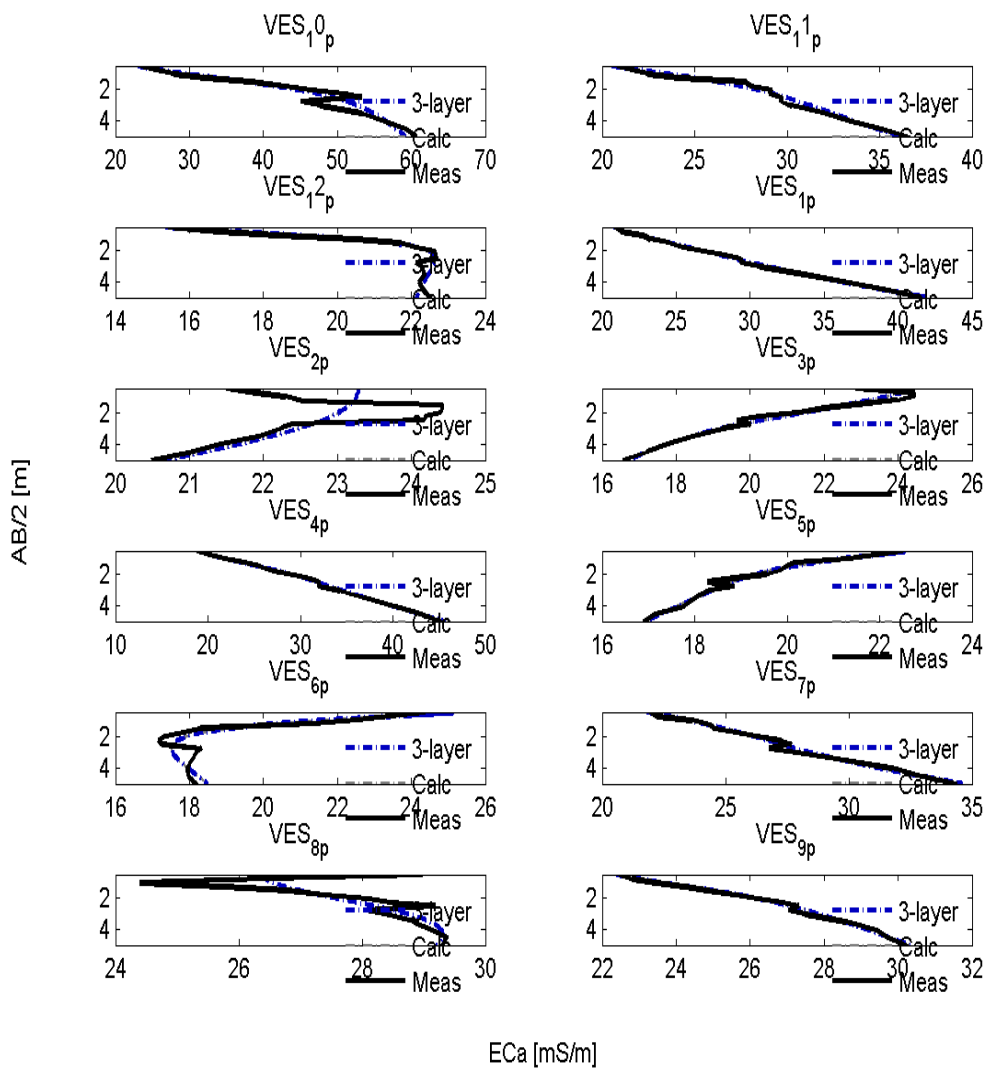


Figure B.2: VES measured and modeled ECa of all 12 locations

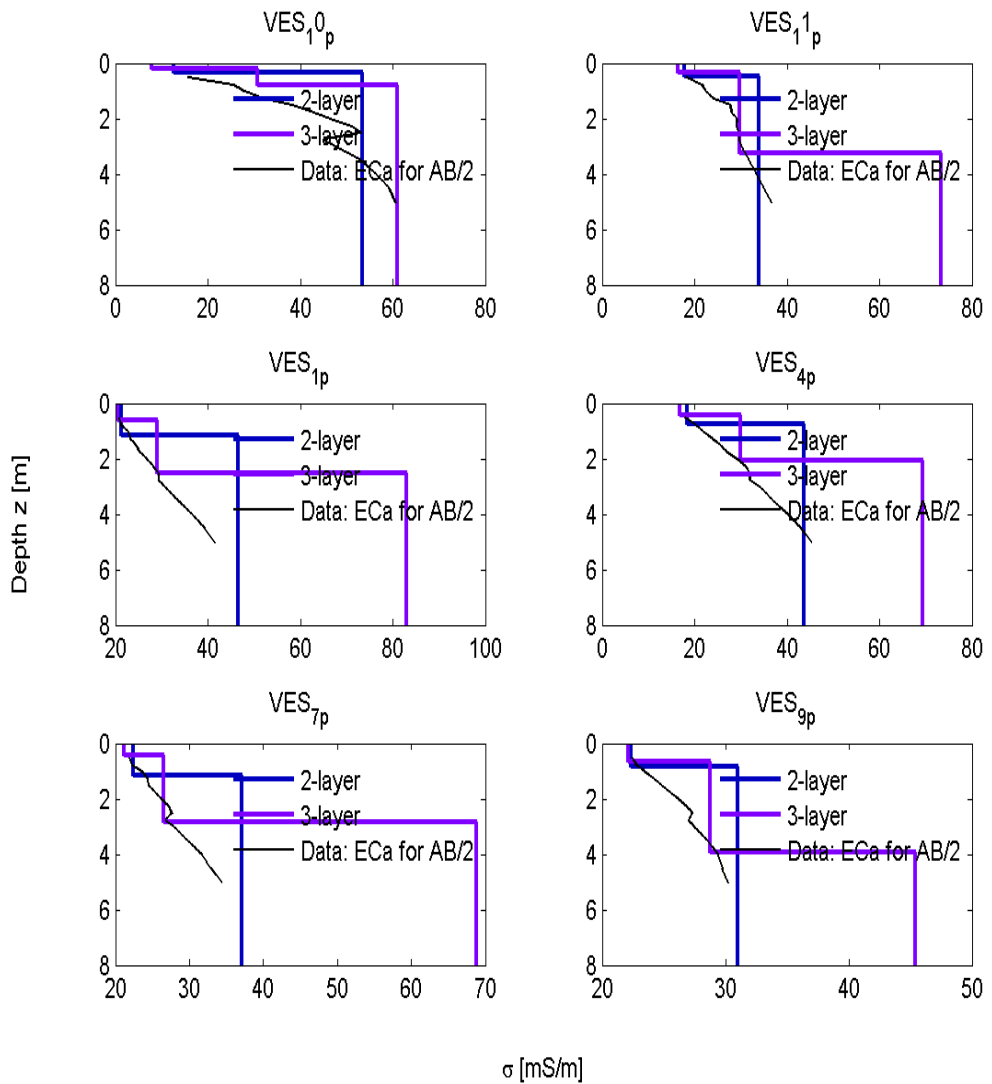


Figure B.3: Underground two and three layer ECa model inversion of all chosen calibration locations

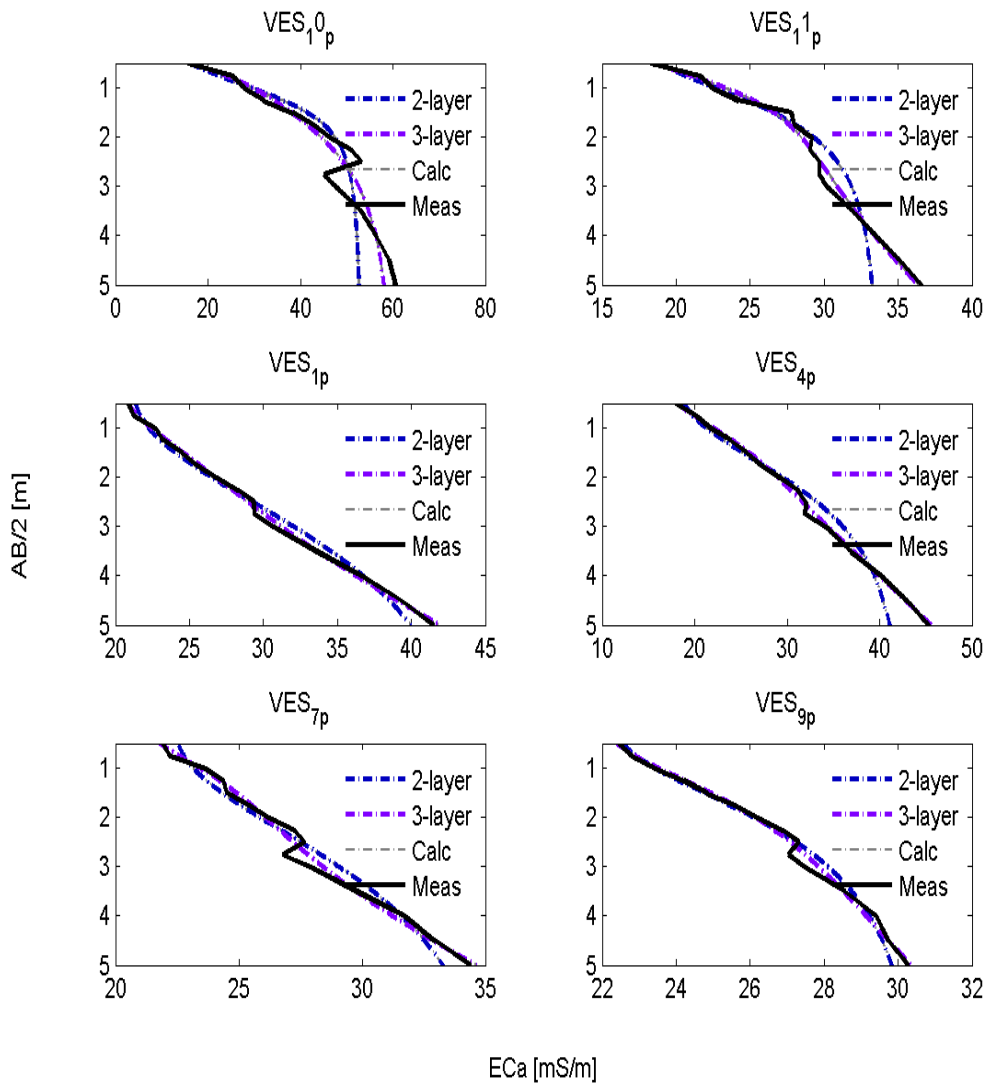


Figure B.4: VES measured and modeled ECa of all chosen calibration locations

C | Large-scale ECa measurement and processing data

C.1 Measurement data of the 10 m and 5 m tracks

C.1.1 Uncalibrated and filtered CMD-MiniExplorer data

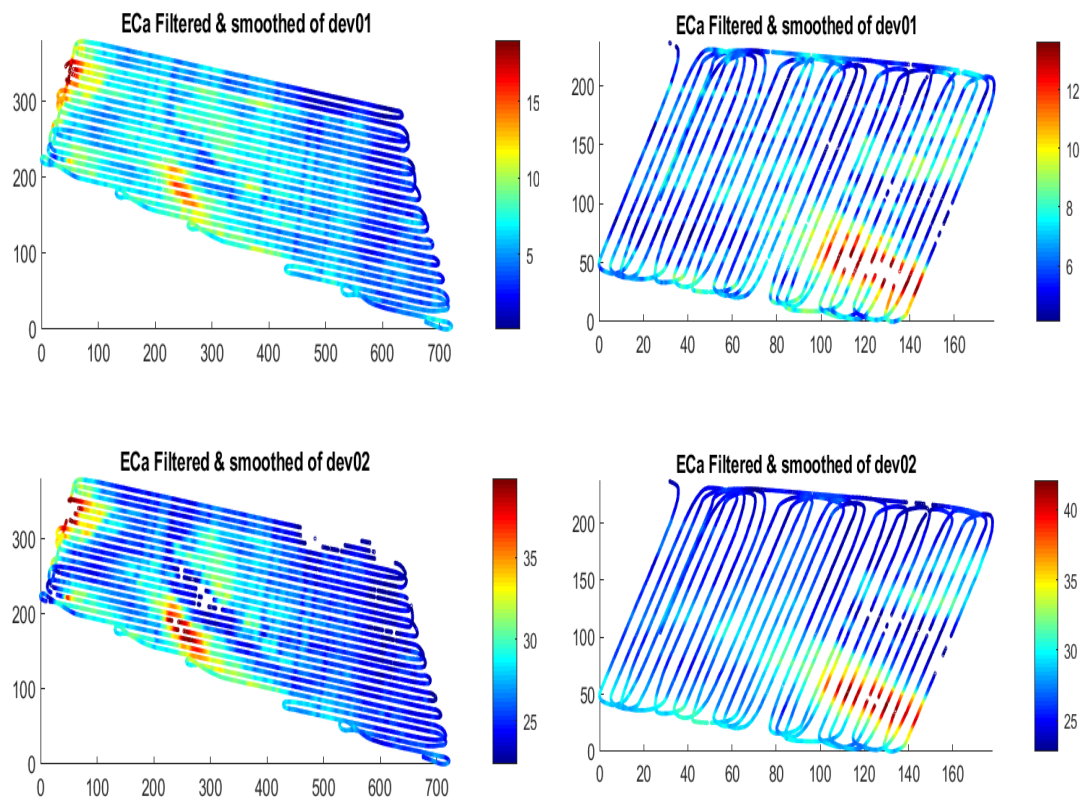


Figure C.1: Uncalibrated and filtered CMD-MiniExplorer 10 m and 5 m Tracks dev1 = HCP32, dev2 = HCP71

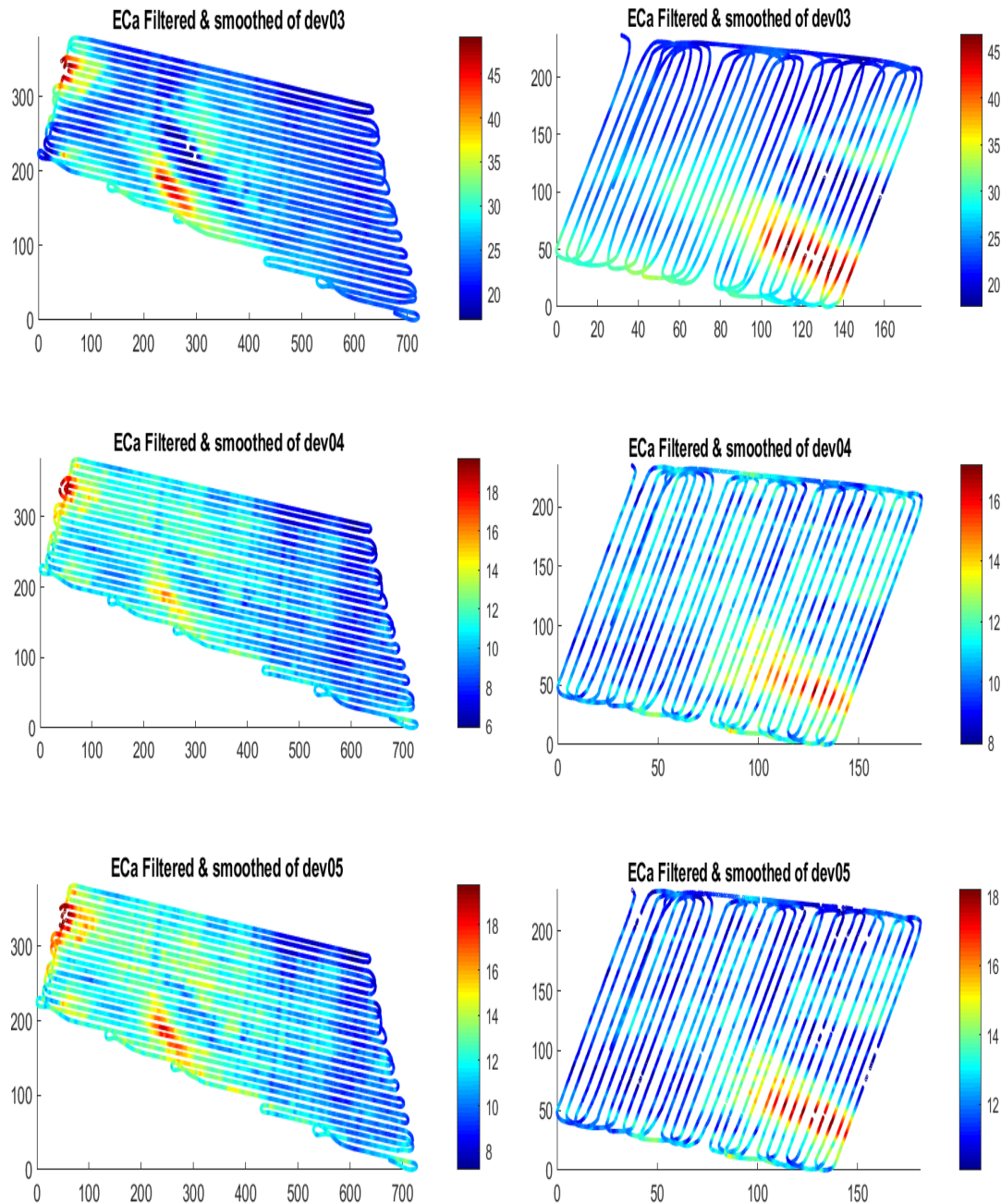


Figure C.2: Uncalibrated and filtered CMD-MiniExplorer 10 m and 5 m Tracks dev3 = HCP118, dev4 = VCP35, dev5 = VCP49

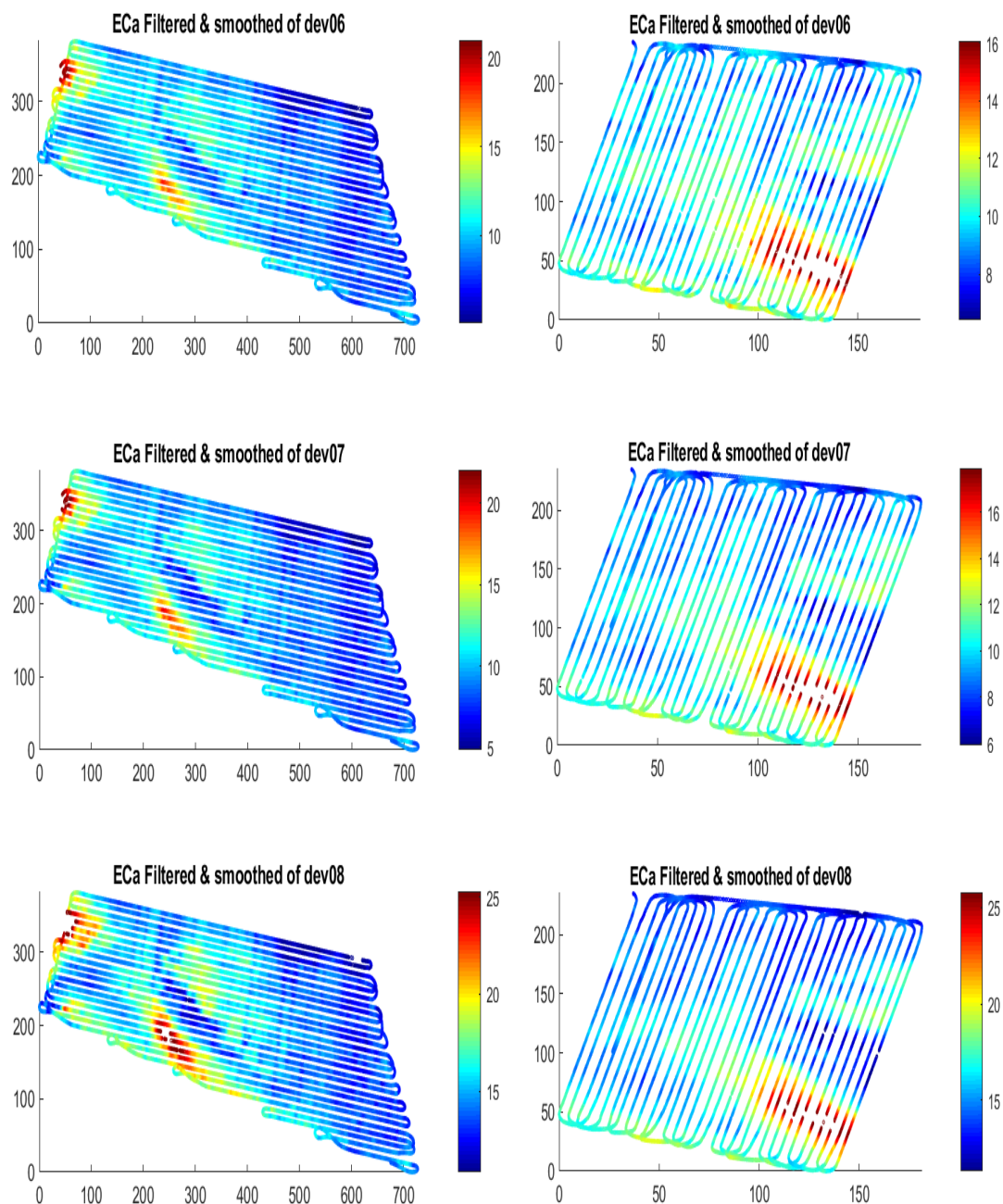


Figure C.3: Uncalibrated and filtered CMD-MiniExplorer 10 m and 5 m Tracks dev6 = VCP71, dev7 = VCP97, dev8 = VCP135

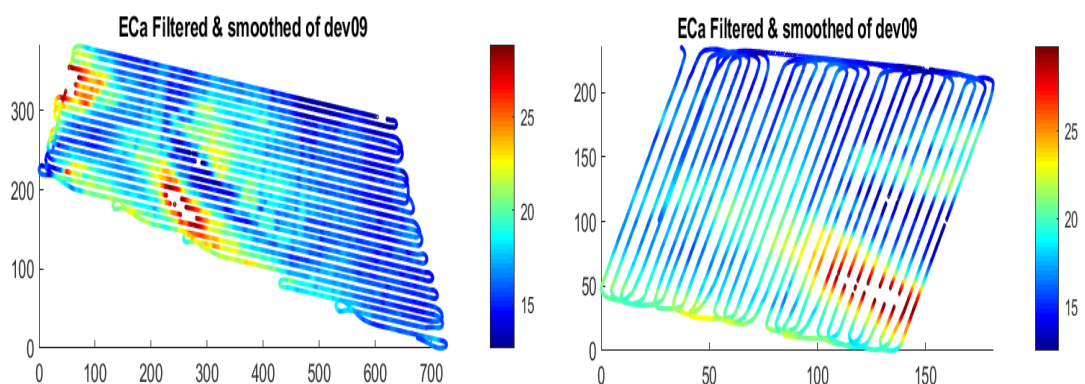


Figure C.4: Uncalibrated and filtered CMD-MiniExplorer 10 m and 5 m Tracks dev6 = VCP180

C.1.2 Topsoil Mapper

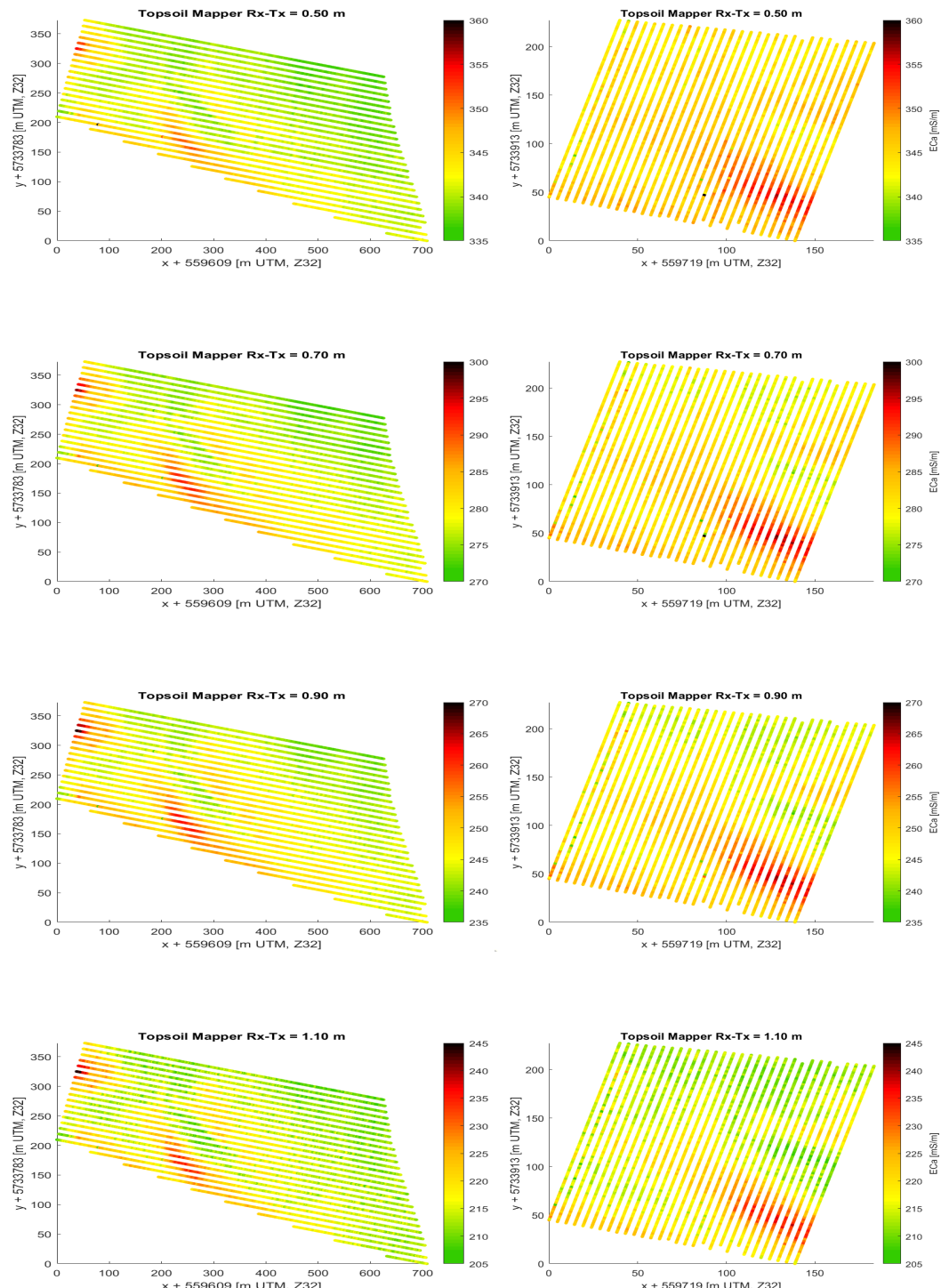


Figure C.5: Uncalibrated 10 m and 5 m plots of the Topsoil Mapper

C.1.3 Geophilus

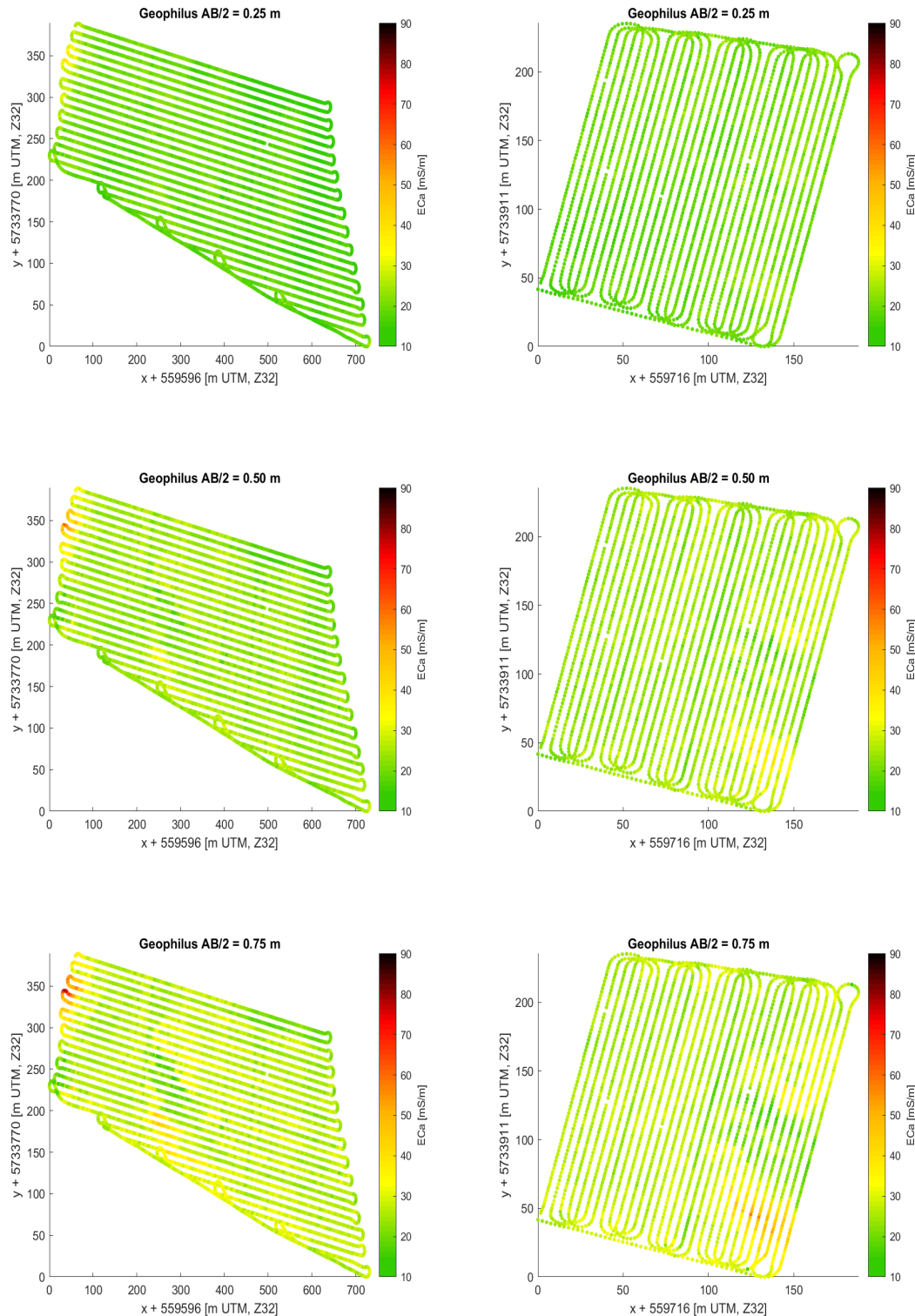


Figure C.6: Uncalibrated 10 m and 5 m plots of the Geophilus, $AB/2 = 0.25$, 0.50 and 0.75 m

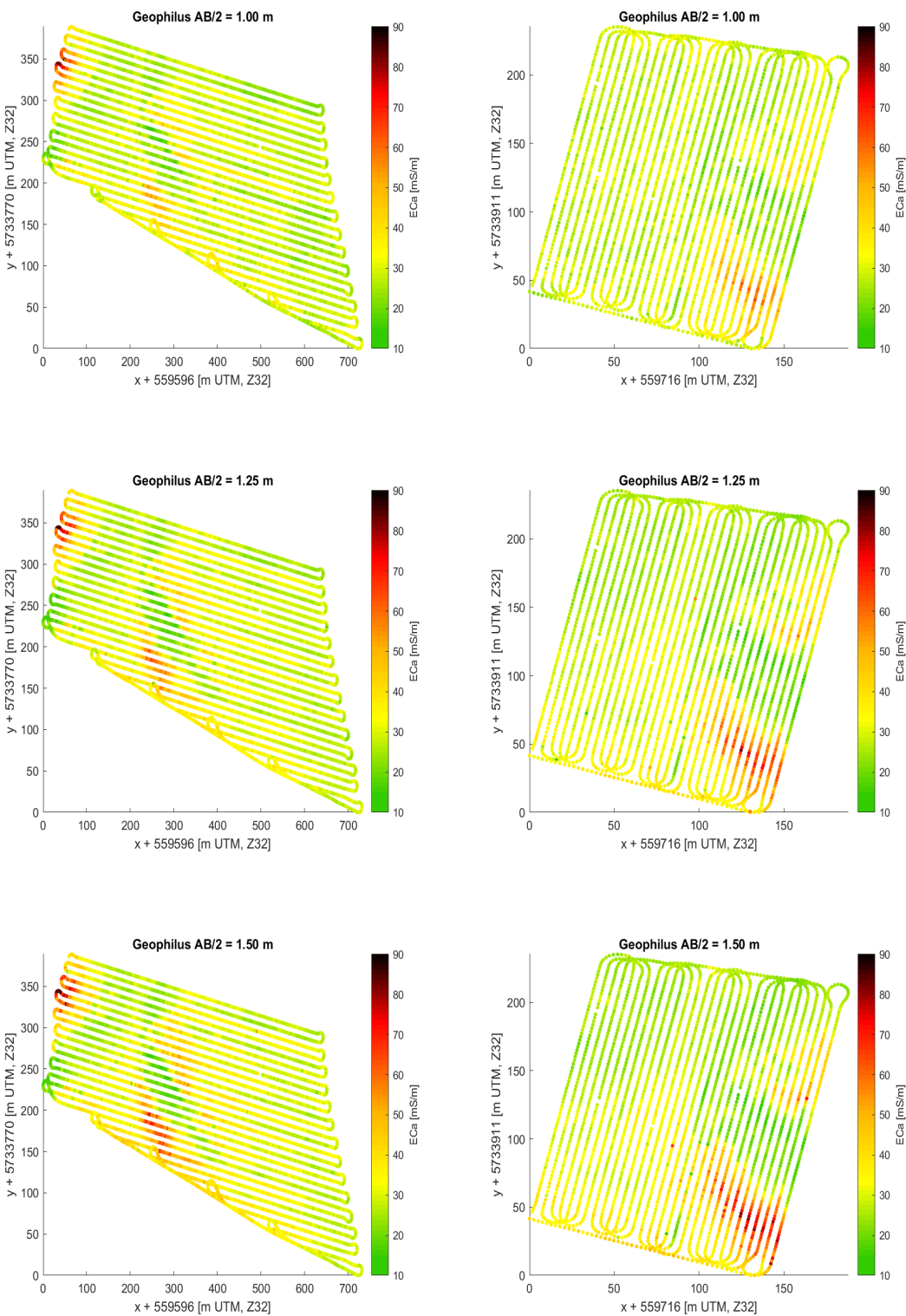


Figure C.7: Uncalibrated 10 m and 5 m plots of the Geophilus, AB/2 = 1.00, 1.25 and 1.50 m

C.1.4 VerisU3 Soil Scanner

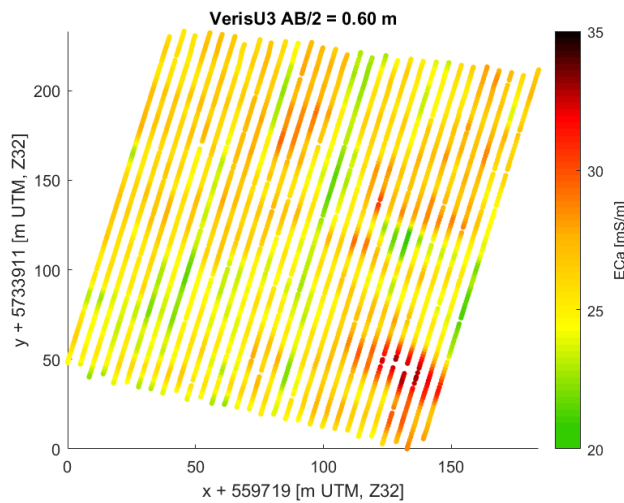


Figure C.8: Uncalibrated 5 m plot of the VerisU3

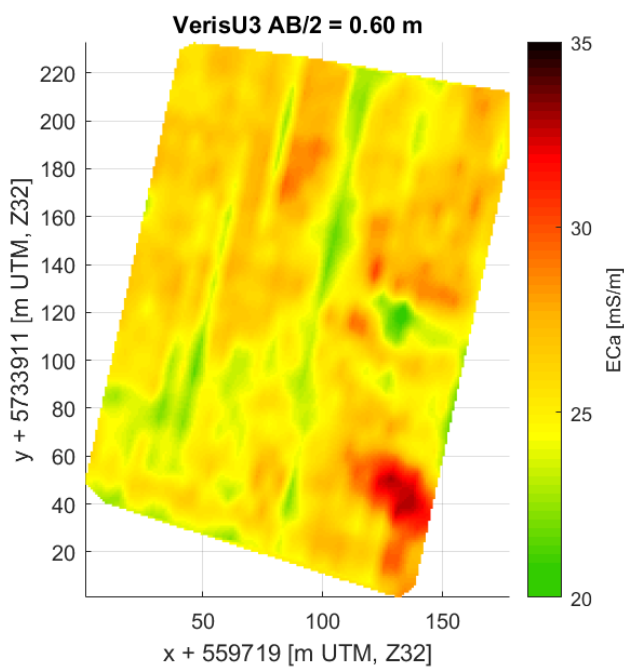


Figure C.9: Uncalibrated 5 m interpolated plot of the VerisU3

C.2 Interpolated 10 m and 5 m track data

C.2.1 Calibrated CMD-MiniExplorer Data

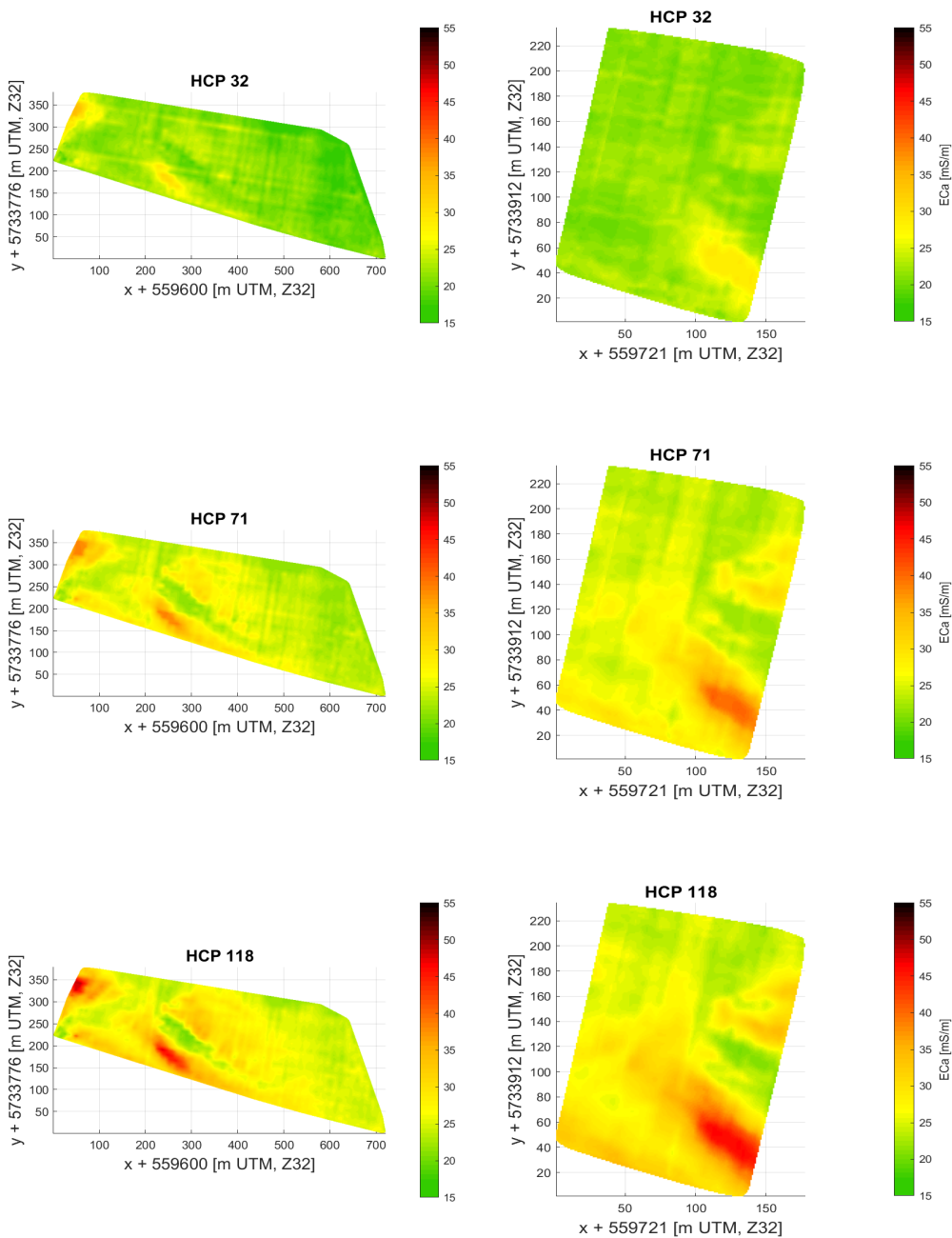


Figure C.10: Calibrated and interpolated 10 m and 5 m track data of the CMD-MiniExplorer, HCP Configurations

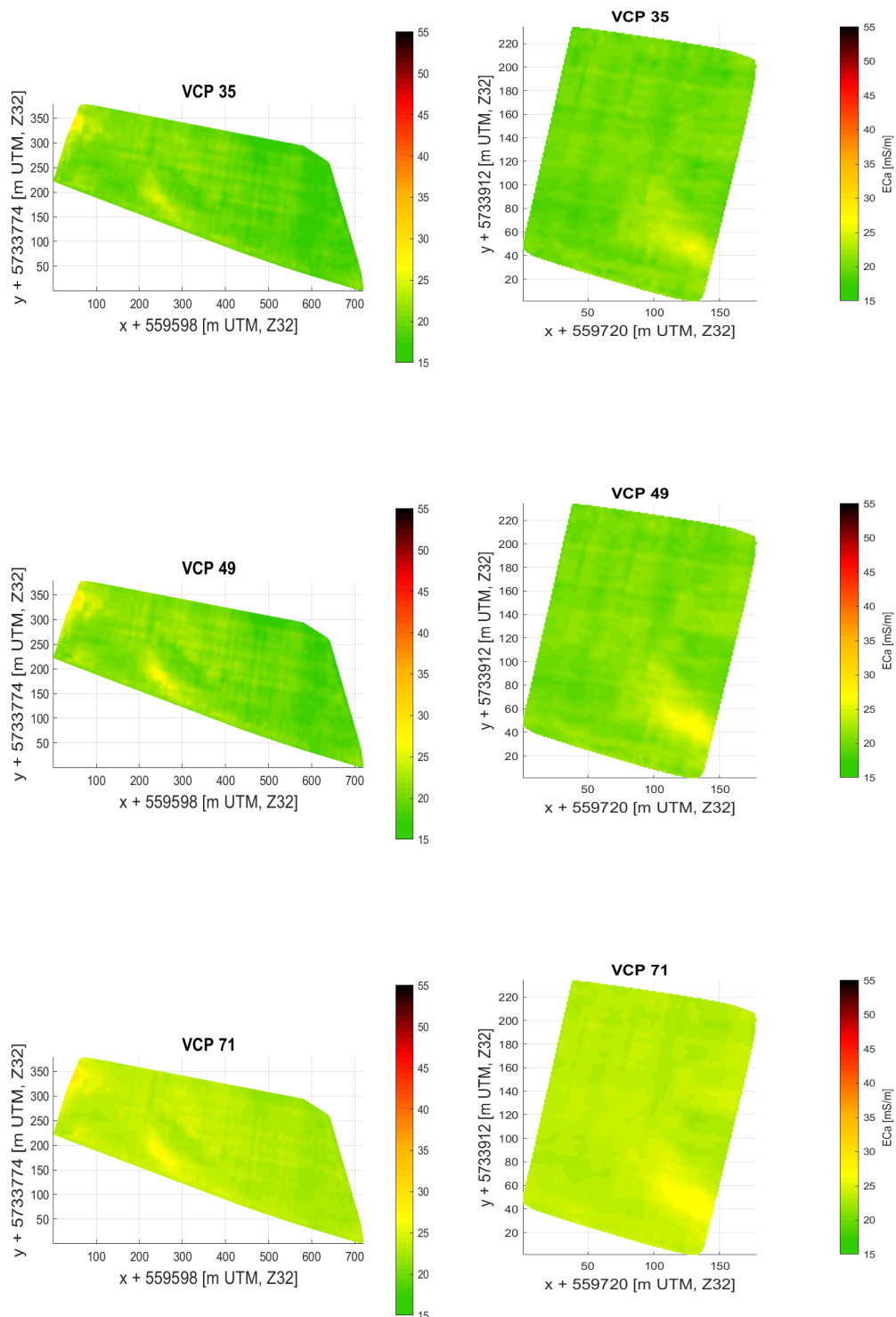


Figure C.11: Calibrated and interpolated 10 m and 5 m track data of the CMD-MiniExplorer, VCP configurations part 1

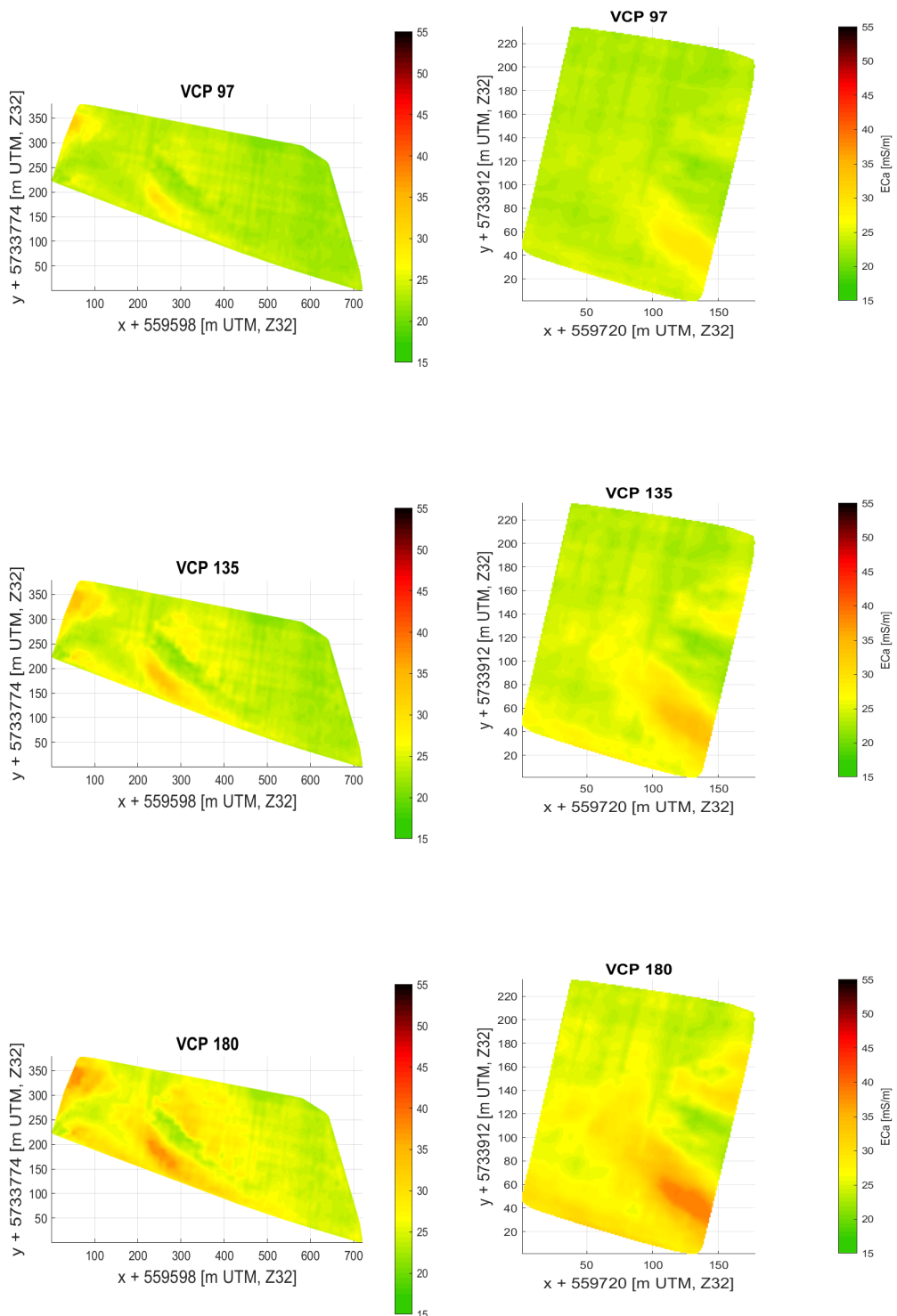


Figure C.12: Calibrated and interpolated 10 m and 5 m track data of the CMD-MiniExplorer VCP configurations part 2

C.2.2 Topsoil Mapper

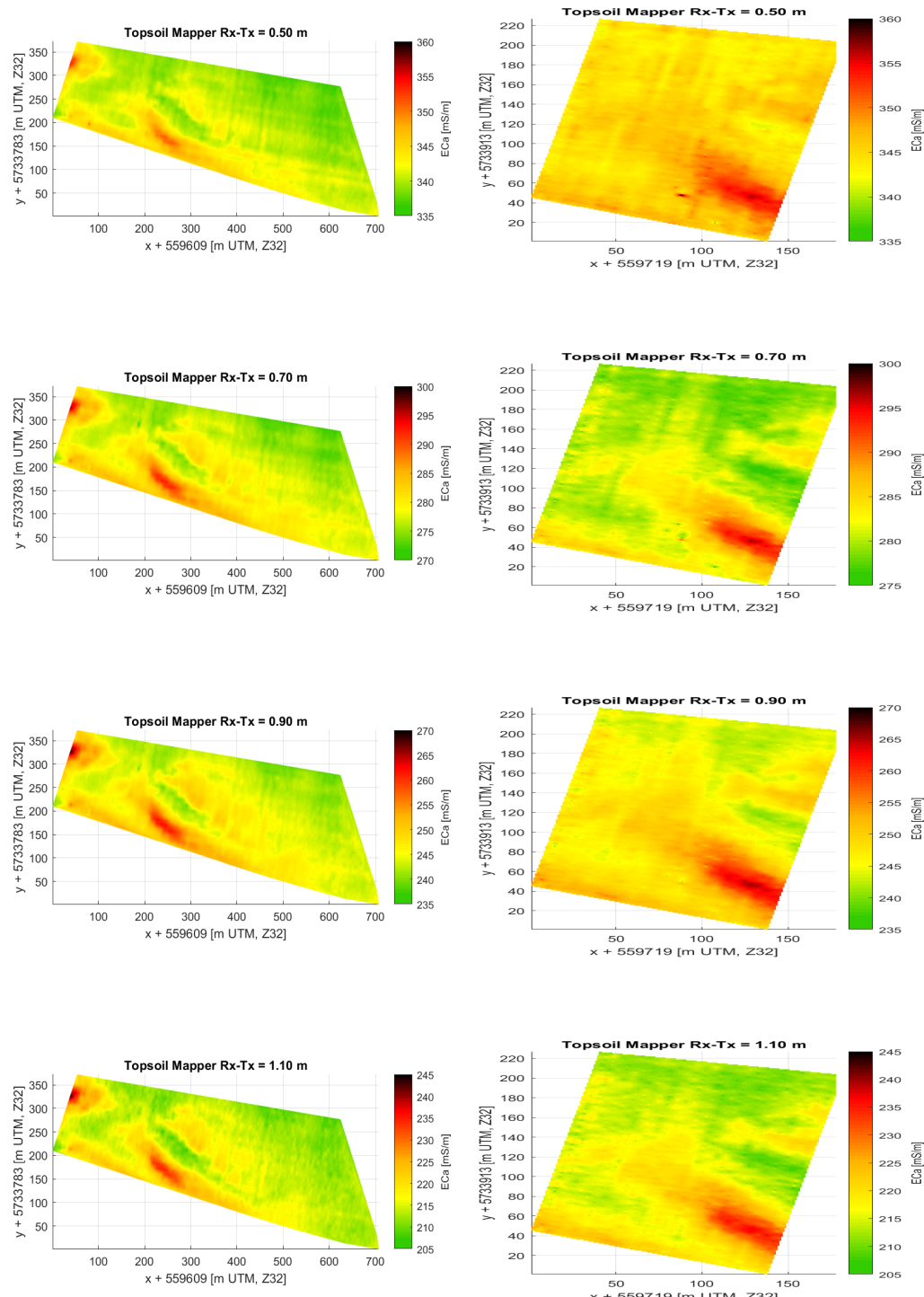


Figure C.13: Interpolated 10 m and 5 m track data of the Topsoil Mapper

C.2.3 Geophilus

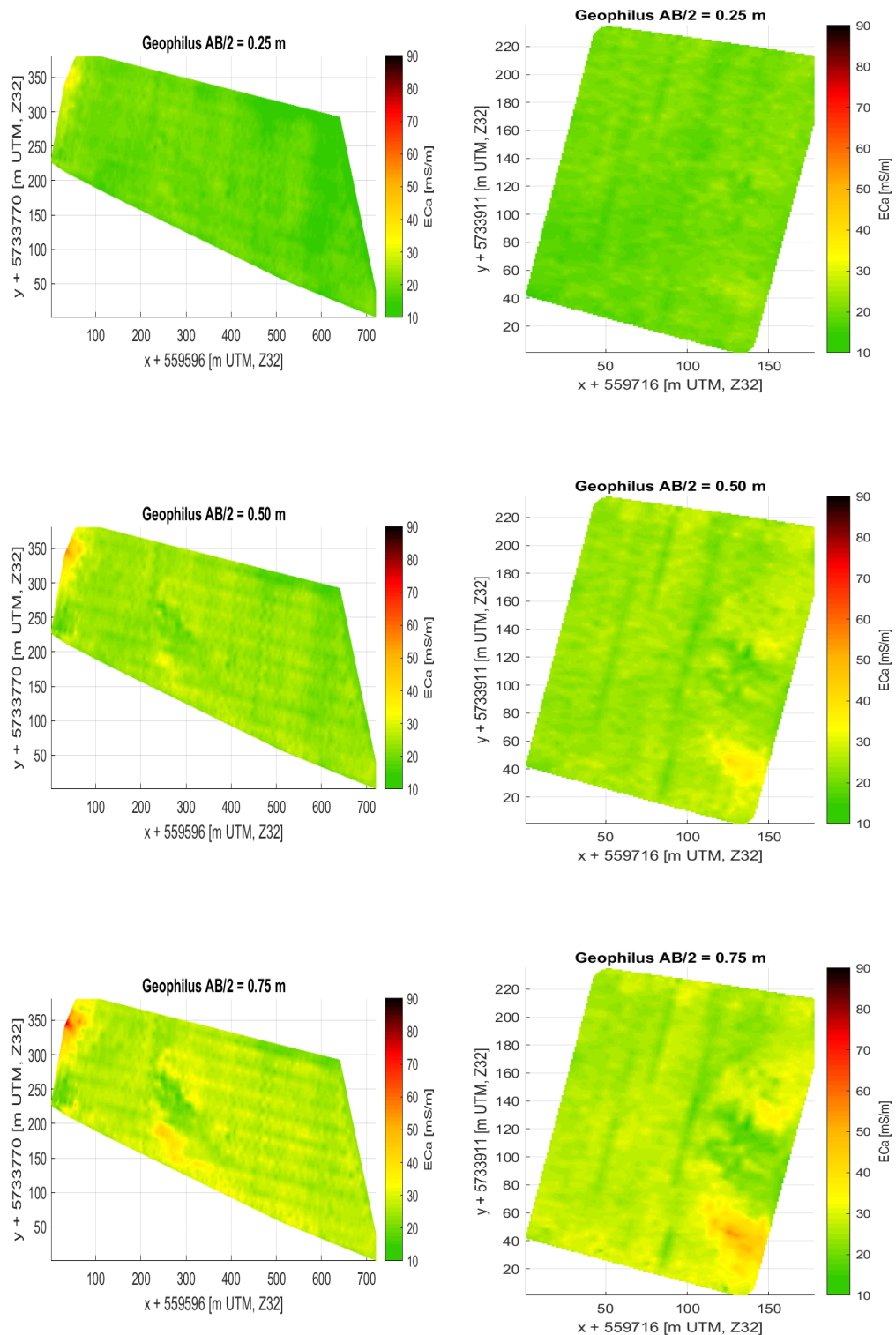


Figure C.14: Interpolated 10 m and 5 m track data of the Geophilus, part 1

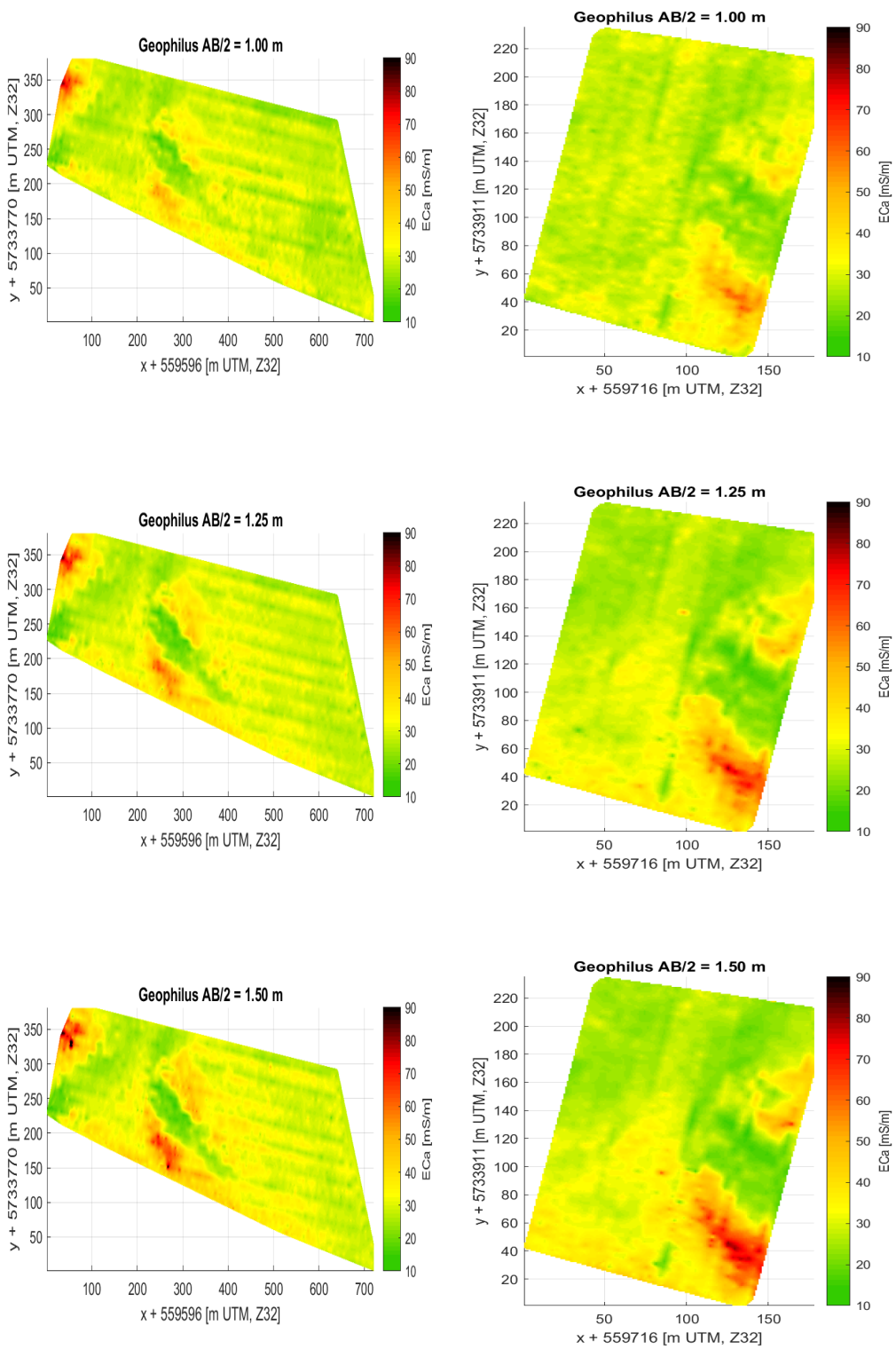


Figure C.15: Interpolated 10 m and 5 m track data of the Geophilus, part 2

C.3 Difference Plots of the interpolated track data

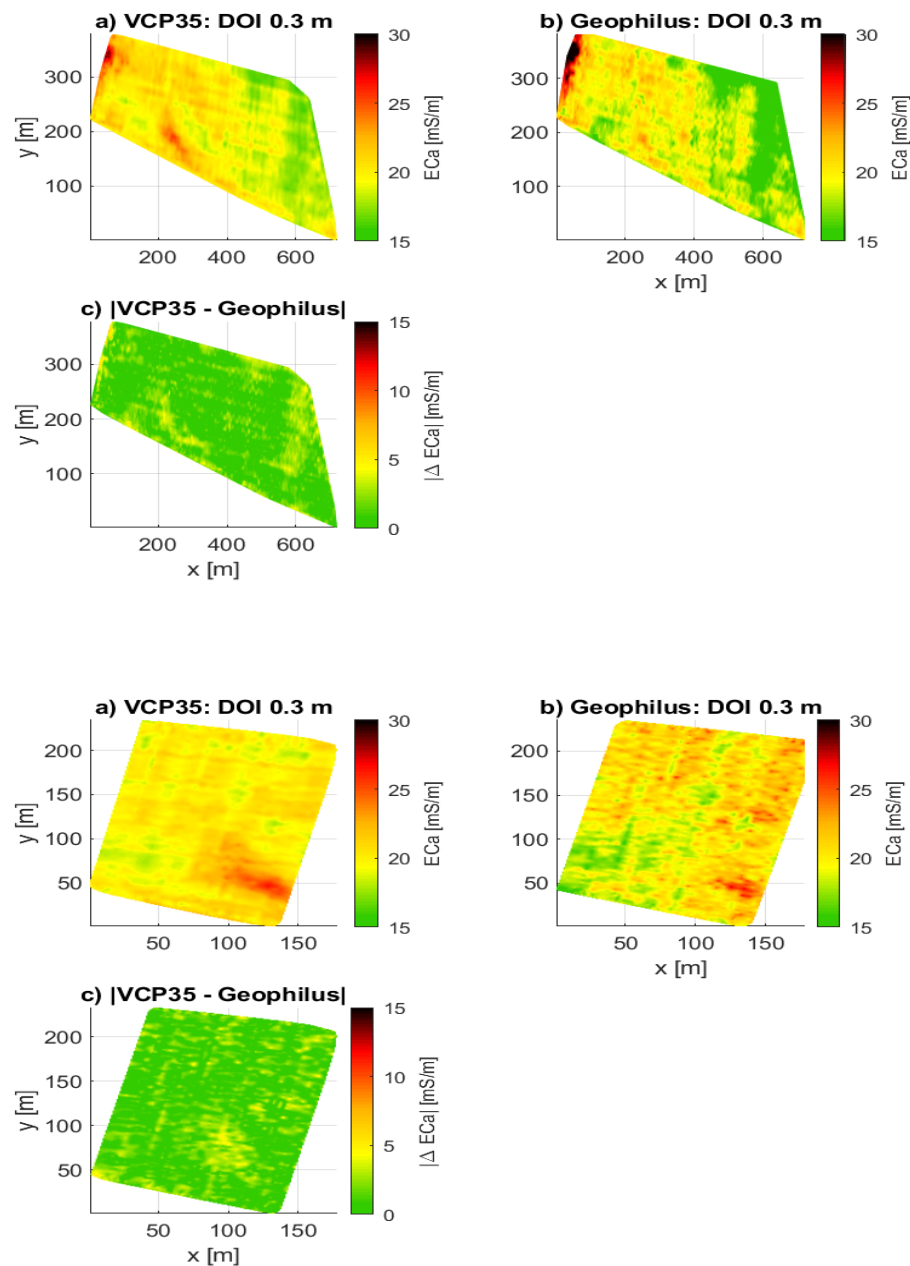


Figure C.16: Difference plot between CMD and Geophilus, DOI 0 - 0.25 m

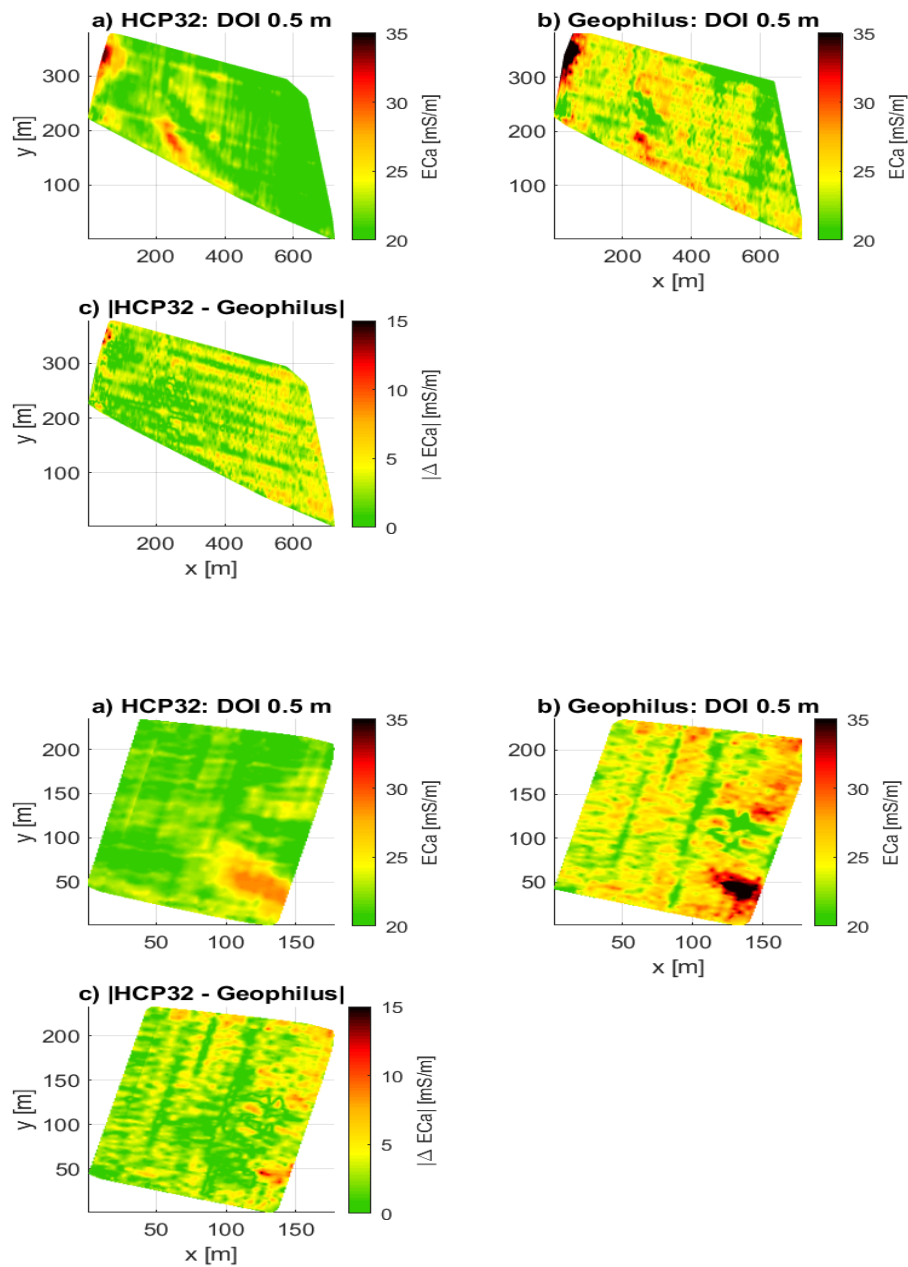


Figure C.17: Difference plot between CMD and Geophilus, DOI 0 - 0.5 m

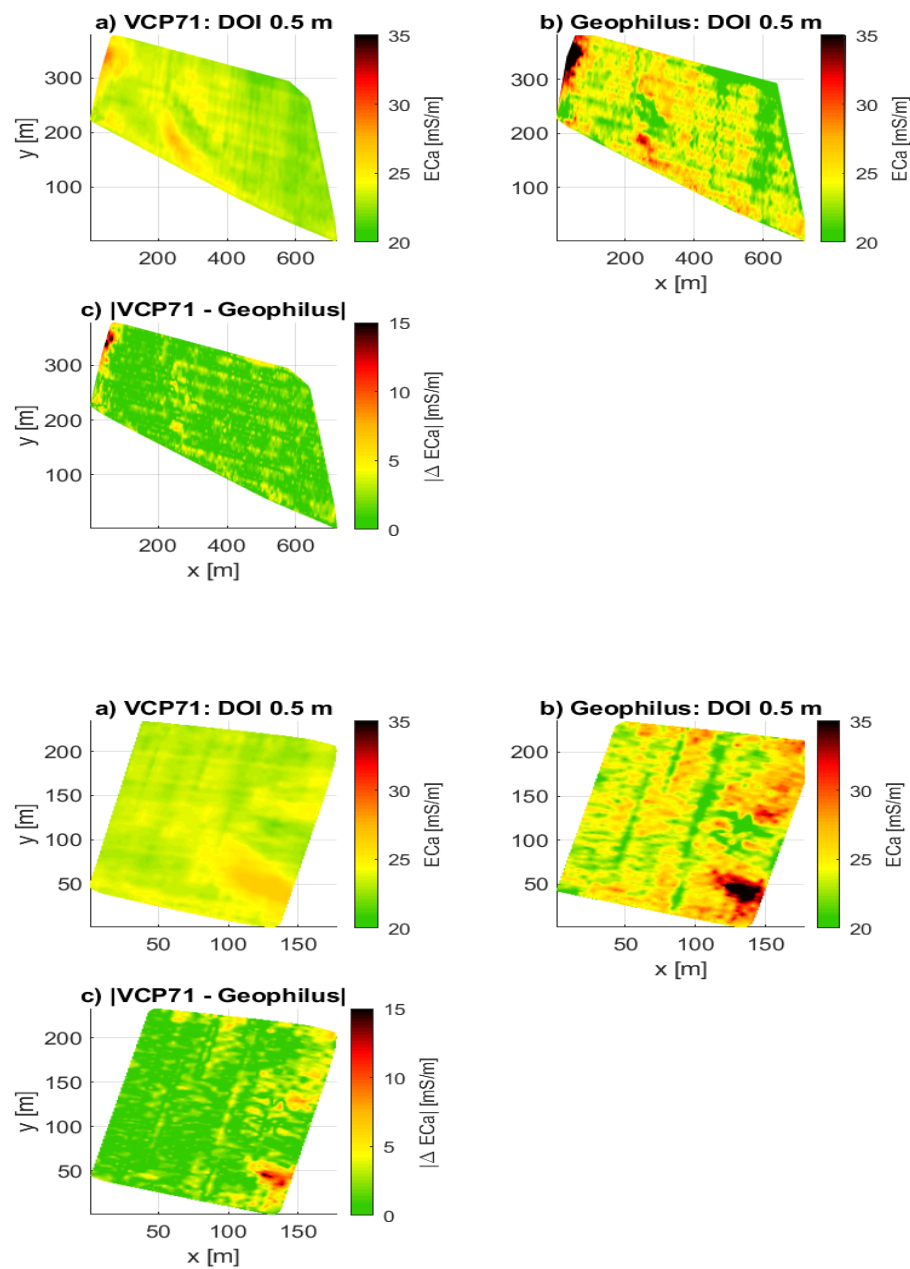


Figure C.18: Difference plot between CMD and Geophilus, DOI 0 - 0.5 m

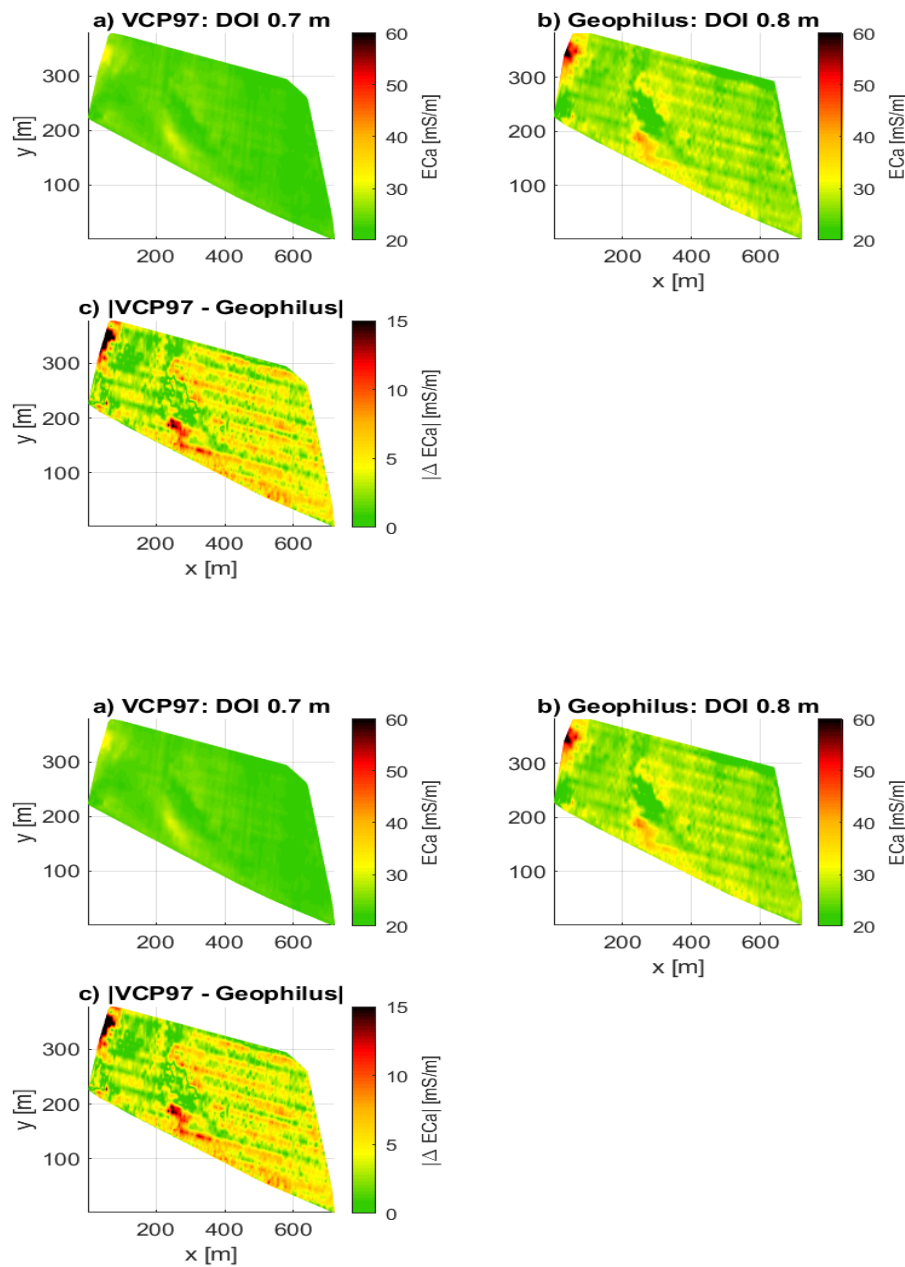


Figure C.19: Difference plot between CMD and Geophilus, DOI 0 - 0.75 m

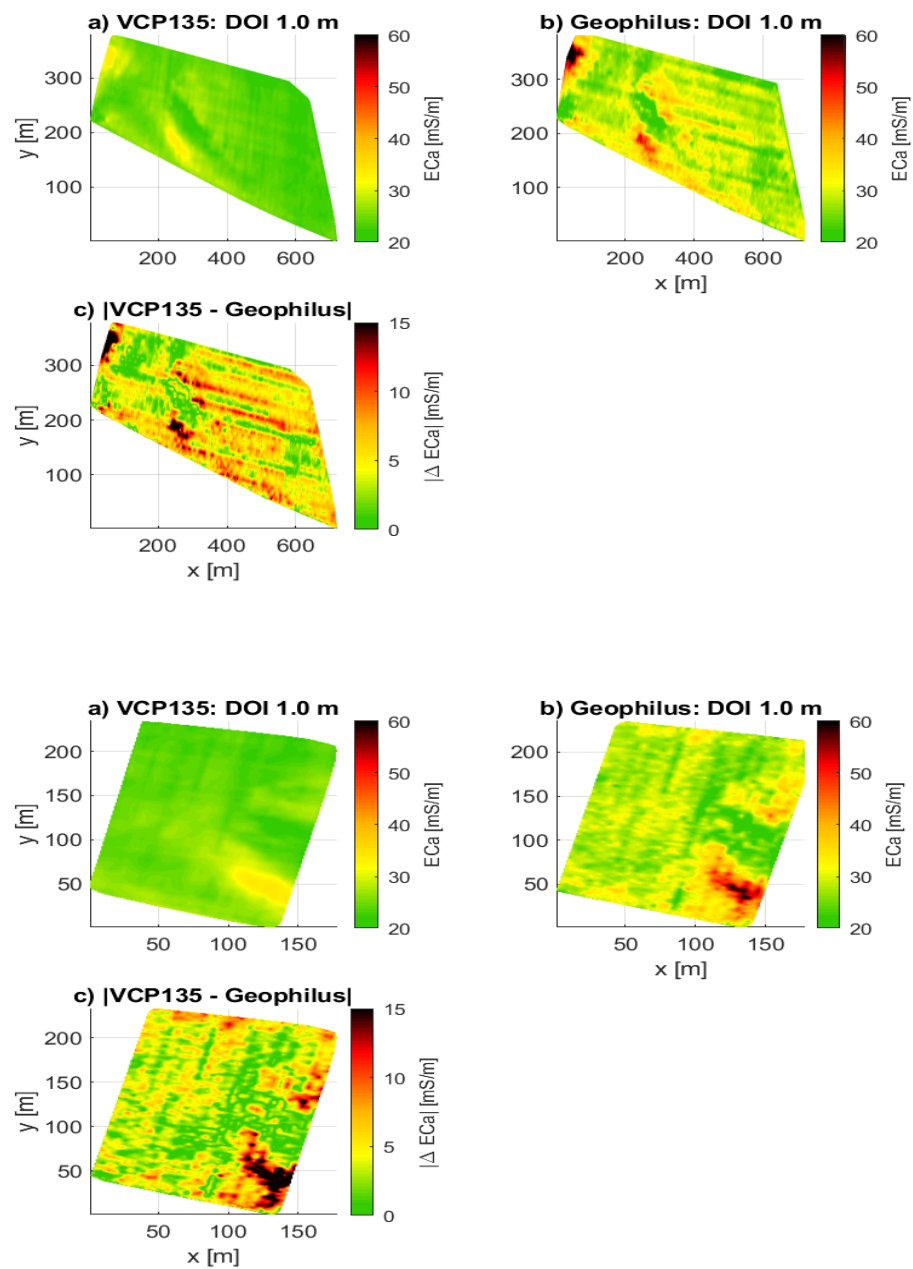


Figure C.20: Difference plot between CMD and Geophilus, DOI 0 - 1.00 m

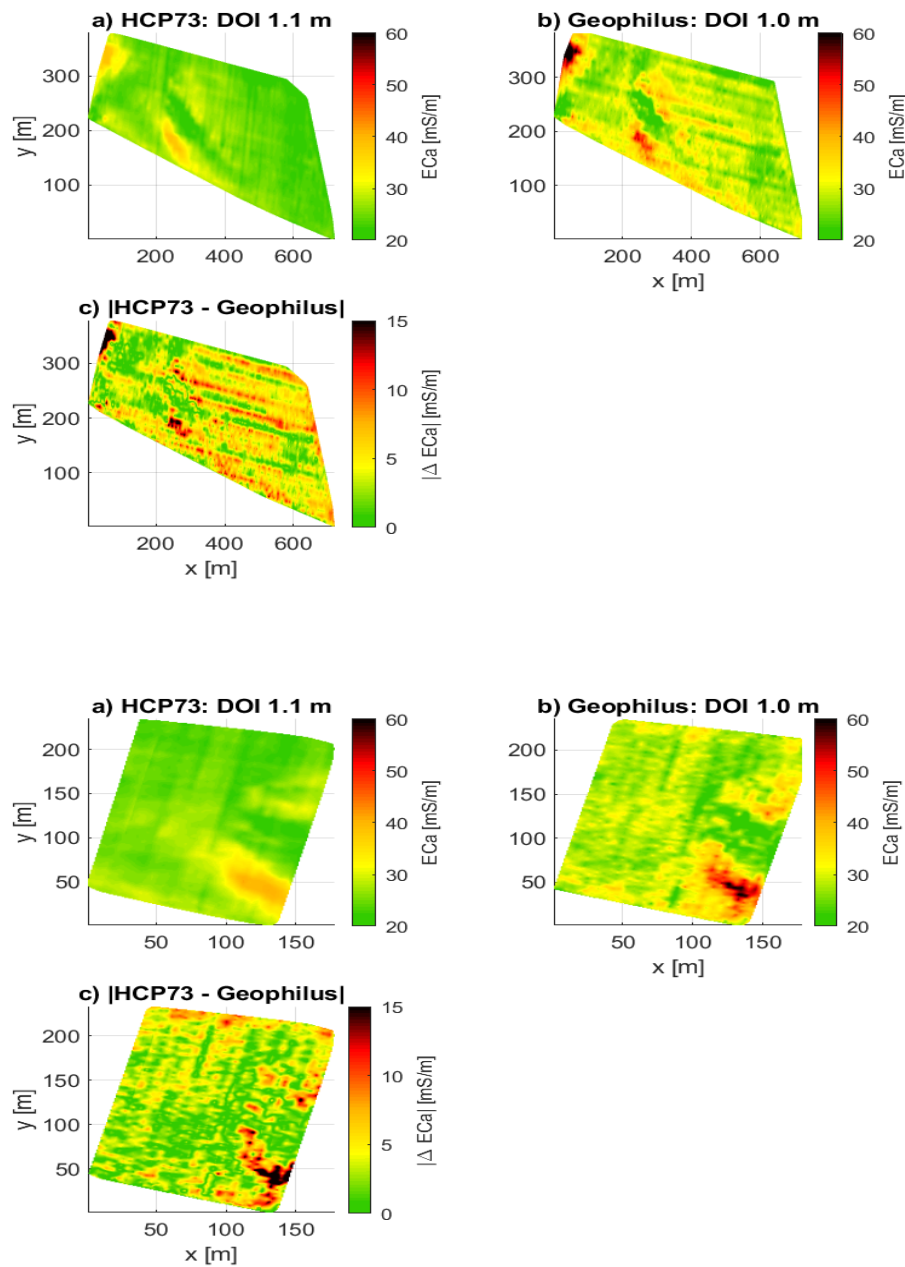


Figure C.21: Difference plot between CMD and Geophilus, DOI 0 - 1.00 m

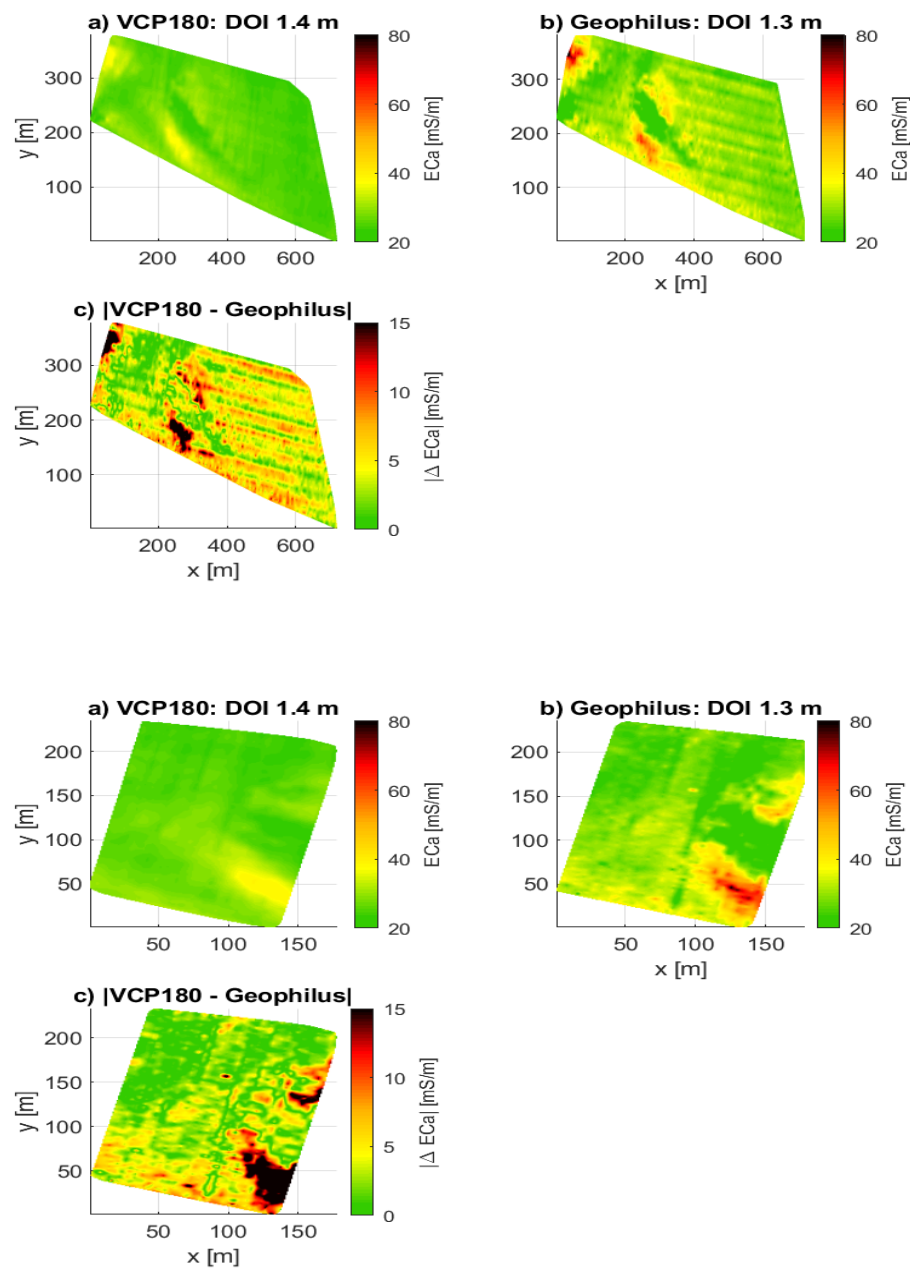


Figure C.22: Difference plot between CMD and Geophilus, DOI 0 - 1.30 m

C.4 Photos of the EMI and DC systems and survey pictures



Figure C.23: Field picture of the CMD-MiniExplorer sleds



Figure C.24: CMD-MiniExplorer sleds attached to the tractor



Figure C.25: Field picture of the Topsoil Mapper



Figure C.26: Distance between the Topsoil Mapper and the tractor



Figure C.27: Field picture of the Geophilus



Figure C.28: Field picture of the VerisU3

List of Figures

2.1	Principle of electromagnetic induction methods [Breidenstein, 2017]	6
2.2	Graphic description of the a) HCP and b) VCP configurations. (S = coil spacing, Tx = transmitter coil, Rx = receiver coil) and local sensitivity functions for depth normalized to coil separation for c) HCP and d) VCP. (after McNeill [1980])	7
2.3	a) Depth investigation characteristics of various array configurations [Roy and Apparo, 1971], b) electrode configuration for a Schlumberger and c) an equatorial Dipole-Dipole array)	10
3.1	Satellite images of the test site taken on a) the 10th of June 2018 and b) the 31th of December 2000 (Google Earth)	12
3.3	Grain size distributions of the soil samples sorted by depth	12
3.2	a) soil type map based on the national BK25 map and b) grain distribution map based on the national GK25 map, scale 1:25000	13
4.1	Sketch of the construction of both sledges and their DOIs	16
4.2	Sketch of the Geophilus construction and its DOIs	18
4.3	Sketch of the disc positions of the VerisU3	19
4.4	Sketch of the principle of VES measurements. Every step the electrode spacing increases increasing the DOI	20
4.5	Map of the Einbeck test site showing the tracks of the EMI and DC measurements and the VES locations	21

5.1	Linear regression of VES ECa predicted (x-axis) and EMI ECa measured values (y-axis) in [mS/m] for all coil configurations	26
5.2	ECa distribution of the 10 m tracks of VCP35, DOI 0 - 0.26 m (above) and HCP118, DOI 0 - 1.77 m (below)	28
5.3	ECa distribution of the Topsoil Mappers 10 m tracks, above: Rx-Tx 0.5 m, DOI 0 - 0.45 m, below Rx-Tx 0.9 m, DOI 0 - 1.05 m	30
5.4	ECa distribution of the Geophilus 10 m tracks, above DOI = 0 - 0.5 m, below DOI = 0 - 1.5 m	31
5.5	ECa distribution of the VerisU3 5 m tracks, DOI = 0 - 0.6 m	32
5.6	Above: difference plot between CMD and Geophilus, DOI 0 - 0.5 m, Below: Difference plot between CMD and VerisU3, DOI 0 - 0.6 m	34
5.7	Vertical standard deviations of the CMD-MiniExplorer (above) and the Geophilus (below)	37
A.1	Picture of the Sedimat 4-12 (UGT 2019)	47
A.2	Cross plot between the clay contents and the ECa of the sleds	50
B.1	Underground three layer ECa model inversion of all 12 locations	51
B.2	VES measured and modeled ECa of all 12 locations	52
B.3	Underground two and three layer ECa model inversion of all chosen calibration locations	53
B.4	VES measured and modeled ECa of all chosen calibration locations	54
C.1	Uncalibrated and filtered CMD-MiniExplorer 10 m and 5 m Tracks dev1 = HCP32, dev2 = HCP71	55
C.2	Uncalibrated and filtered CMD-MiniExplorer 10 m and 5 m Tracks dev3 = HCP118, dev4 = VCP35, dev5 = VCP49	56
C.3	Uncalibrated and filtered CMD-MiniExplorer 10 m and 5 m Tracks dev6 = VCP71, dev7 = VCP97, dev8 = VCP135	57
C.4	Uncalibrated and filtered CMD-MiniExplorer 10 m and 5 m Tracks dev6 = VCP180	58
C.5	Uncalibrated 10 m and 5 m plots of the Topsoil Mapper	59

C.6 Uncalibrated 10 m and 5 m plots of the Geophilus, AB/2 = 0.25, 0.50 and 0.75 m	61
C.7 Uncalibrated 10 m and 5 m plots of the Geophilus, AB/2 = 1.00, 1.25 and 1.50 m	62
C.8 Uncalibrated 5 m plot of the VerisU3	63
C.9 Uncalibrated 5 m interpolated plot of the VerisU3	63
C.10 Calibrated and interpolated 10 m and 5 m track data of the CMD- MiniExplorer, HCP Configurations	64
C.11 Calibrated and interpolated 10 m and 5 m track data of the CMD- MiniExplorer, VCP configurations part 1	65
C.12 Calibrated and interpolated 10 m and 5 m track data of the CMD- MiniExplorer VCP configurations part 2	66
C.13 Interpolated 10 m and 5 m track data of the Topsoil Mapper	67
C.14 Interpolated 10 m and 5 m track data of the Geophilus, part 1	69
C.15 Interpolated 10 m and 5 m track data of the Geophilus, part 2	70
C.16 Difference plot between CMD and Geophilus, DOI 0 - 0.25 m	71
C.17 Difference plot between CMD and Geophilus, DOI 0 - 0.5 m	72
C.18 Difference plot between CMD and Geophilus, DOI 0 - 0.5 m	73
C.19 Difference plot between CMD and Geophilus, DOI 0 - 0.75 m	74
C.20 Difference plot between CMD and Geophilus, DOI 0 - 1.00 m	75
C.21 Difference plot between CMD and Geophilus, DOI 0 - 1.00 m	76
C.22 Difference plot between CMD and Geophilus, DOI 0 - 1.30 m	77
C.23 Field picture of the CMD-MiniExplorer sleds	78
C.24 CMD-MiniExplorer sleds attached to the tractor	78
C.25 Field picture of the Topsoil Mapper	79
C.26 Distance between the Topsoil Mapper and the tractor	80
C.27 Field picture of the Geophilus	80
C.28 Field picture of the VerisU3	81

LIST OF FIGURES

List of Tables

4.1	Coil characteristics of the sleds	16
4.2	Coil characteristics of the Topsoil Mapper	17
4.3	Electrode spacings AB and its respective DOIs	18
4.4	The VerisU3 electrode spacing AB and its respective DOI	19
4.5	Electrode spacings used for the VES measurements	19
5.1	Applied parameters for the shift correction	26
5.2	Vertical changes of mean ECa and standard deviations [mS/m]	35
5.3	Mean CMD and Geophilus ECa and standard deviations [mS/m] of similar DOIs [m]	35
5.4	Mean CMD and VerisU3 ECa and standard deviations [mS/m] of similar DOIs [m]	36
5.5	Vertical changes of mean ECa and standard deviations [mS/m] of both DC systems	36
A.1	Grain size distributions of calibration locations 1 - 6	48
A.2	Grain size distributions of calibration locations 7 - 12	49